

Technical Report

**TR-17-13**

November 2018



POSKBAR project

# Development, testing and application of alternative models for bentonite expansion and erosion

**Marcelo Laviña**

**Andrés Idiart**

**Jorge Molinero**

**Guillermo Casas**

SVENSK KÄRNBRÄNSLEHANTERING AB

SWEDISH NUCLEAR FUEL  
AND WASTE MANAGEMENT CO

Box 3091, SE-169 03 Solna  
Phone +46 8 459 84 00  
skb.se

SVENSK KÄRNBRÄNSLEHANTERING



ISSN 1404-0344

**SKB TR-17-13**

ID 1604377

November 2018

**POSKBAR project**

# **Development, testing and application of alternative models for bentonite expansion and erosion**

Marcelo Laviña, Andrés Idiart, Jorge Molinero  
Amphos 21 Consulting S. L.

Guillermo Casas, CIMNE

This report concerns a study which was conducted for Svensk Kärnbränslehantering AB (SKB) and Posiva Oy. The conclusions and viewpoints presented in the report are those of the authors. SKB or Posiva may draw modified conclusions, based on additional literature sources and/or expert opinions.

A pdf version of this document can be downloaded from [www.skb.se](http://www.skb.se).

© 2018 Svensk Kärnbränslehantering AB



## Summary

A study of bentonite swelling and eroding processes is presented. After hydration and saturation, the bentonite buffer under repository conditions can be at some point locally unconfined due to the existence of transmissive fractures traversing the deposition hole. The report includes a preliminary assessment of these processes using two different and complementary state-of-the-art approaches. The first one characterises bentonite erosion using a particle-based approach. Although several numerical tools have been developed to adapt existing CFD-DEM (computational fluid dynamics and discrete element models), this approach still yields unreasonable computational costs. As an alternative, an intermediate approach is also proposed, consisting of studying upscaled properties for the macroscopic description of the system. The second approach is based on classical soil mechanics models. These models are used to simulate the first stages of bentonite swelling and extrusion into a transmissive fracture. However, their range of applicability does not include the state of the material at which erosion takes place. The results presented underline the potentials and limitations of the modelling approaches applied to the assessment of bentonite erosion.

## Sammanfattning

Rapporten presenterar en studie av bentonitsvällning och erosions processer. Efter hydratisering och mättnad kan bentonitbufferten under förvarsförhållanden vid någon tidpunkt, lokalt, befinna sig i ett läge där den kan svälla fritt, på grund av förekomsten av transmissiva sprickor som passerar deponeringshålet. Rapporten innehåller en preliminär bedömning av dessa processer med hjälp av två olika och kompletterande state-of-the-art-metoder. Den första karakteriserar bentoniterosion med hjälp av ett partikelbaserat tillvägagångssätt. Även om flera numeriska verktyg har utvecklats för att anpassa befintliga CFD-DEM (beräknad vätskedynamik och diskreta elementmodeller), ger detta tillvägagångssätt fortfarande orimliga beräkningskostnader. Som ett alternativ föreslås ett mellanliggande tillvägagångssätt, bestående av att studera uppskalade egenskaper för den makroskopiska beskrivningen av systemet. Det andra tillvägagångssättet är baserat på klassiska jordmekanikmodeller. Dessa modeller används för att simulera de första stegen av bentonitsvällning och extrudering i en transmissiv spricka. Däremot omfattar deras tillämpningsområde inte tillståndet för det material vid vilket erosion äger rum. De presenterade resultaten understryker potentialen och begränsningarna av modelleringsmetoderna som används vid bedömningen av bentoniterosion.

## Acknowledgements

The authors would like to acknowledge Sergio Samat for his contribution and support regarding the soil mechanics models implemented in Code\_Bright. Constructive comments from both reviewers are also gratefully acknowledged.



# Contents

<b>1</b>	<b>Introduction</b>	9
<b>2</b>	<b>Literature review</b>	11
2.1	Modelling Approaches	11
2.1.1	Dynamic bentonite diffusion: the “rim model”	11
2.1.2	Expansive soil mechanics models	13
2.2	Available experiments	14
2.2.1	Free swelling experiment	14
2.2.2	Swelling and erosion in an artificial fracture	14
2.3	Concluding remarks	15
<b>3</b>	<b>Application of particle-based approach to the study of bentonite erosion</b>	17
3.1	Continuum models	17
3.1.1	Mass conservation equation	17
3.1.2	Diffusivity function	18
3.1.3	Results and known limitations of the continuum models	19
3.1.4	Further critique	20
3.2	Analysis of scales	20
3.2.1	Extent of rim zone	20
3.2.2	Time to steady-state	22
3.3	Discrete element model	23
3.3.1	Basic Ingredients	23
3.3.2	Equation of motion for the particles	24
3.3.3	Contact model	26
3.3.4	Time integration scheme	27
3.4	Direct approach	29
3.4.1	Boundary conditions	29
3.4.2	Computational cost	31
3.5	Recovering the macroscopic diffusivity	34
3.5.1	Filtering	34
3.5.2	Derivative Recovery	35
3.5.3	Calculating the diffusivity	36
3.6	Future developments	38
3.6.1	The need for further developments	38
3.6.2	Realistic particle shapes and the study of flocculation	38
3.6.3	Hydrodynamic interactions	38
3.6.4	Coarse Graining	39
3.6.5	Boundary conditions	40
3.6.6	The possibility of implicit time stepping	40
3.7	Concluding Remarks & Outlook	40
<b>4</b>	<b>Simulation of experimental tests with a soil mechanics model</b>	41
4.1	Modelling approach	41
4.2	Free swelling test I	42
4.2.1	Model setup	42
4.2.2	Results	43
4.3	Free swelling test II	44
4.3.1	Model setup	44
4.3.2	Results	45
4.4	Erosion in a fracture test	45
4.4.1	Model setup	47
4.4.2	Results	49
<b>5</b>	<b>Conclusions and discussion</b>	53
5.1	Conclusions of particle-based models	53

5.2	Conclusions of experiments and soil mechanics models	53
5.3	Multi-phase bentonite modelling based on macroscopic models as a potential way forward	54
	<b>References</b>	55
<b>Appendix A</b>	Analysis of the formulation proposed by Neretnieks et al. (2017)	59

# 1 Introduction

Upon hydration and saturation, the bentonite buffer of a KBS 3V repository swells within a deposition hole, filling the gap between the partially-saturated buffer and the rock. Once filled, bentonite develops a swelling pressure, counteracted by the stiffness of the walls of the deposition hole. However, bentonite is not fully confined in the deposition hole. This is due to the fact that bentonite could swell into transmissive fractures traversing the deposition hole, which are actually the paths through which groundwater saturates the buffer. This unconfined situation may lead to the erosion of bentonite, provided specific conditions are met. In recent years, these conditions, and the physical and chemical mechanisms governing bentonite erosion from the buffer of a KBS 3V repository, have been given a lot of attention (e.g. Grindrod et al. 1999, Birgersson et al. 2009, Neretnieks et al. 2009, Moreno et al. 2010, Schatz et al. 2013). The reason is the potential impact on long-term performance of compacted bentonite under repository conditions. After a glacial event, groundwater composition at repository depth could have a very low ionic strength. In such an event, the risk is that a large mass of bentonite could be eroded. The treatment of erosion in current safety cases considers that a significant mass loss of bentonite can occur under specific conditions, impairing the buffer performance. In those cases, failure of the copper canisters by corrosion is considered possible, which could have a significant impact on the safety assessment of the repository. Therefore, a better understanding of the processes involved would serve to consider less pessimistic approaches that treat bentonite erosion based on a more mechanistic approach of the problem.

An EU dedicated project (named BELBaR project; <http://www.skb.se/belbar/>) on bentonite erosion has been recently completed. Several experimental and modelling studies were conducted within the framework of this research project. As a result, the erosion models that have been used by SKB and Posiva in recent long-term safety assessments for the final repository for spent nuclear fuel have been further developed and refined. The refined model can be transformed into a relatively simple mathematical expression that can be used for quantitative assessments. However, there are still large uncertainties dealing with the parameterisation and processes considered in the refined model. It is thought that further development and verification would be needed to increase the confidence in the use of such modelling approach for predictive purposes.

The main objective of the new project, named POSKBAR, is to develop and implement alternative models to quantify the mass loss of bentonite from the buffer and backfill due to erosion. In particular, such models need to capture the main features of colloid formation and gel destabilisation when dilute groundwater reaches the repository. For that purpose, the POSKBAR project is divided into two phases: (1) a first phase for testing, verifying and identifying weaknesses in current models, using laboratory data and knowledge primarily from the BELBaR project, and (2) a second phase for the development of an updated model that can be used to quantify the mass loss of bentonite in a situation where dilute groundwater reaches the repository.

The main objectives of the present study are:

1. To implement nano-/micro-meter processes in a particle-based discrete element model in the Kratos Multiphysics framework (Dadvand et al. 2010) to investigate some of the key parameters used in the model by Neretnieks et al. (2017).
2. To evaluate the feasibility of coupling the Neretnieks et al. (2017) “rim model” for bentonite erosion with macroscopic soil-mechanics expansion models of bentonite.

The achievements concerning the first objective are reported in Section 3. The associated work has been developed in cooperation with the International Centre for Numerical Methods in Engineering (CIMNE) in Barcelona, Spain. The work related with the second objective is in turn reported in Section 4.

A brief literature review is first presented in Section 2, considering key publications related with bentonite erosion models and experimental data available for future testing of modelling approaches. Scientific literature related with the application of particle-based discrete models to colloids, is reviewed in Section 3, which is relevant to macroscopic mechanics of bentonite expansion. The intention is to evaluate the main hypotheses used in current modelling approaches as a basis for

establishing and proposing potential improvements or alternative methods. The goal is to pinpoint where the particle methods and/or macroscopic soil mechanics models may intervene to:

- a. support key hypotheses and assumptions,
- b. modify/enrich them,
- c. enhance the system understanding of the expansion and erosion processes, and
- d. reproduce existing experiments.

Section 3 describes the work related with the novel development of a particle-based model to simulate the bentonite gel/sol interaction at nano-/micro-meter scale. This work has been performed in cooperation with the International Centre for Numerical Methods in Engineering (CIMNE). A first attempt is presented to use the particle-based model to help identifying specific issues in the current formulation (Neretnieks et al. 2017) that could be enriched, corrected or confirmed, by dedicated simulations. The particle-based model is implemented in the Kratos Multiphysics framework (Dadvand et al. 2010), using the existing discrete element-based module Swimming DEM Application. The development and verification includes:

- a. All the force potentials relevant to the formulation of Liu et al. (2009a) of the bentonite gel/sol.
- b. One-way coupled hydrodynamic interaction that can deal with the extremely low Stokes numbers of the flow.

The particle-based model is used to evaluate the underlying hypotheses of the model developed by Neretnieks et al. (2017). Some of these hypotheses have already been identified by those authors as being in the need of such scrutiny (e.g. hypotheses concerning flocculation). The work developed in this study focuses on the rim zone, i.e. the thin outermost layer of the expanding clay gel/sol. The viscosity in this zone decreases markedly, which makes bentonite in this region to be more susceptible to drag forces by the incoming flow. The methodology presented here focuses on the microscopic scale using particle-based methods to simulate a representative volume element (RVE). This RVE is assumed to contain a sufficiently large number of clay particles, which are then explicitly subjected to the interaction laws, as opposed to Neretnieks et al. (2017), who considered these laws at a larger scale of analysis. This work is reported in Section 3 of the current document.

A first feasibility study is then presented in Section 4 to conceptualise and simulate the expansion of bentonite using soil mechanics theory (e.g. Alonso et al. 1999, Navarro et al. 2014). Recently, Navarro et al. (2016) proposed an approach for simulating the coupled processes of swelling and mechanical erosion of compacted MX-80 bentonite. The loss of mass at the water-soil interface is described by means of a simplified erosion model, assuming an “instantaneous activation” of erosion. A double-porosity formulation is considered to describe the mechanical behaviour of bentonite. The authors claimed that satisfactory representation of experimental data can be obtained by simulating a variety of pinhole tests on MX-80 samples of various configurations. In the present study, a soil mechanics model is used to study the expansion of compacted swelling bentonite into a fracture using the finite element code Code\_Bright (Olivella et al. 1996). The main goal is to assess the feasibility of analysing the erosion of bentonite using a traditional hydro-mechanical approach based on the Barcelona expansive model for bentonite (Alonso et al. 1999, Pinyol et al. 2007).

## 2 Literature review

The current design of a KBS 3 repository type for spent nuclear fuel relies upon the use of compacted bentonite clay as buffer material due to its low permeability at full saturation and high swelling capacity. As mentioned in the introduction (Section 1), upon full saturation bentonite develops a swelling pressure against the rock wall of the deposition tunnel. This swelling capacity is a key feature to ensure long-term performance of the engineered barrier and needs therefore to be correctly characterised. Open fractures traversing the deposition hole, through which groundwater flows and saturates the buffer, represent pathways through which bentonite can swell under free conditions. The brief literature review presented here summarises some key features, models and experiments of bentonite erosion, mainly extracted from the BELBaR project.

Under repository conditions, saturated compacted bentonite with a dry density of around 1 700 kg/m<sup>3</sup> has a swelling pressure in the order of tens of MPa. In the presence of fractures, the buffer material can swell into these spaces, potentially decreasing the density and swelling pressure. Density can highly decrease generating a bentonite with only 20 % volume fraction of smectite and still a swelling pressure in the range of 0.03 to 0.3 MPa (Neretnieks et al. 2009).

Swelling is highly dependent on the ionic strength of the surrounding water and the porewater. The critical coagulation concentration parameter (CCC), establishes the critical value at which swelling stops. Below the CCC bentonite continues to swell and the gel turns into a sol. Smectite clay swells in fractures taking up water until a stable sol is formed. For high ion concentrations, not a sol but a gel with no particle release is generated (Birgersson et al. 2009, Neretnieks et al. 2017). At the interface with the seeping water, colloids are formed and transported away by water in fractures.

The responsible of these special features of bentonite is the structure of its main mineral, montmorillonite, which in MX-80 bentonite accounts for more than 80 wt. %. The clay mineral particles are very thin coin like sheets, 1 nm thick and 50 to 500 nm long. Between these sheets, there is an interlayer water with a very high ionic strength (2-3 M), developing very large repulsive forces.

The following review is centred on the main and most recent modelling approaches and the available set of experiments where these processes are quantified.

### 2.1 Modelling Approaches

Bentonite erosion has traditionally been studied from different points of view or focusing on different processes such as: bentonite gels stability in crystalline rock (Pusch 1983, 1999, 2007), erosion by flowing water (Boisson 1989), erosion in connection with possible retrieval of canisters (Sjöblom et al. 1999), mechanical erosion and colloid formation by flowing groundwater (Grindrod et al. 1999), erosion particles and dispersion-flocculation behaviour of bentonite particles (Kurosawa et al. 1999), long-term behaviour of buffer materials in nuclear waste repositories (Verbeke et al. 1997), or extrusion behaviour of buffer material into fractures using X-ray CT methods (Tanai and Matsumoto 2007).

Since the pioneering work of Liu and Neretnieks (2006), a new approach has been developed focusing on a phenomenological description of chemical and smectite surface processes. Erosion resulting from the rate of colloid generation is addressed in this model with a focus on chemical aspects.

A completely different approach is the model presented by Navarro et al. (2017), which is closer to traditional soil mechanics models. Even though it is based on the classical soil mechanics theory, it also includes some chemical effects.

#### 2.1.1 Dynamic bentonite diffusion: the “rim model”

During the last years, a novel model has been developed by Neretnieks and co-workers at the Department of Chemical Engineering and Technology of KTH to tackle the issue of bentonite erosion. They proposed a model to quantify the rate of bentonite loss from the buffer under repository conditions. The model is based on the equilibrium between net repulsion forces and friction forces

of particles in water, accounting for Brownian motion. The equation that describes the smectite mass balance is similar to the advection-diffusion equation and is given by:

$$\frac{\partial \phi}{\partial t} = -F_g \nabla \left( \frac{\phi}{f} \right) - u \nabla \phi + \nabla \cdot \left( \frac{x}{f} \nabla \phi \right) \quad (2-1)$$

where  $\phi$  ( $\text{m}^3$  bentonite/ $\text{m}^3$  water) is the volume fraction of smectite in the fluid,  $u$  ( $\text{m} \cdot \text{s}^{-1}$ ) is the fluid velocity,  $x$  (J) is the sum of the energy of the particles,  $F_g$  (N) accounts for the gravitational force and the buoyant force, and the factor  $f$  ( $\text{N} \cdot \text{s} \cdot \text{m}^{-1}$ ) considers that smectite moves into the fracture and that an equivalent volume of water moves in the opposite direction. The ratio  $x/f$  can be considered as a diffusivity function.

The dynamic clay expansion model relates the swelling pressure with (1) particle charge, (2) size, (3) smectite volume fraction, (4) ion concentration, and (5) friction against water (Moreno et al. 2010, 2011). Numerical difficulties encountered when applying this model to the simulation of erosion within a fracture promoted the development of an alternative solution method. This new method divides the entire region into two subdomains: the expanding clay region and the rim region.

### Two region model

The release and flow of smectite particles takes place in a very narrow region, where there is a rapid drop in smectite volume fraction ( $\phi$ ) from its value at the rim border ( $\phi_R$ ) to virtually zero. In the region where  $\phi$  is between 0.005 and 0.015 (depending on ion concentration), below  $\phi_R$ , viscosity decreases very strongly with decreasing  $\phi$ . Upstream the rim region the gel is rigid and smectite particles do not flow. The rim region can be very thin compared to the radius of the expanded gel and is computed as a boundary condition to the expanding clay region. The clay entrance from the deposition hole towards the fracture and the loss at the rim are accounted for solving the expanding region. This solution technique results in an expanding model with the rim zone as an external boundary (Neretnieks et al. 2017).

### Diffusivity function

Like molecular diffusion, the expansion of clay and sol formation can be described by a diffusion equation (Liu et al. 2009a, Neretnieks et al. 2009). Although the diffusivity function is essentially constant ( $0.3 \times 10^{-9} \text{ m}^2 \cdot \text{s}^{-1}$  at low sodium ion concentrations and for volume fractions above 0.1), its dependence on ion concentration is crucial for modelling the loss at the rim.

### Viscosity

The viscosity equation used by the authors is based on the model by Liu (2011) and relies upon the notion of co-volume. It follows the idea that when smectite sheets can no longer rotate freely, gel viscosity dramatically increases, as shown in experiments reported in Birgersson et al. (2009).

### Flocculation loss

Based on the work presented in Neretnieks et al. (2010), an expression used for accounting the loss of radionuclides in the interface between seeping water and clay is adapted. The loss at the rim is modelled by the following expression:

$$N_{erosion} = 2N_{rim} = \rho_s \delta \phi_R \cdot 4/\sqrt{\pi} \sqrt{D_R \pi r_R u_0} \quad (2-2)$$

where,  $\rho_s$  is the smectite particle density, the volume fraction of smectite  $\phi_R$  is known,  $D_R$  is the diffusion coefficient at the rim,  $u_0$  the approaching water velocity and  $\pi \cdot r_R$  accounts for the rim boundary length.

### Expansion

The expansion takes place in the inner part of this two-region model, situated between the deposition hole and the rim region. The content of smectite is then a balance accounting for the intrusion from the material in the deposition hole and the loss of particles diffusing out in the moving boundary rim. Expansion is calculated through the dynamic diffusion equation, coupling the volume fraction decreasing with radius and the changes in diffusion coefficient.

### **Pseudo steady-state (PSS)**

Solving the coupled equations of the two-region model in a rigorous is highly time consuming. An alternative solution method approximates the smectite volume fraction profile in the expanding region as the one obtained in its steady-state. Steady-state is defined in this context as the situation in which the mass of intruded bentonite from the deposition hole is equal to the mass loss at the rim.

### **Simplified diffusion function**

An alternative to the PSS computing method is to set a simpler form of the dynamic diffusion equation. The fit is done by considering two distinct diffusivity functions, one for gel-like bentonite and another for colloidal diffusion. This seems a reasonable approximation due to their different behaviours (e.g. Schatz et al. 2013).

## **2.1.2 Expansive soil mechanics models**

Based on the Cam-Clay model (Schofield and Wroth 1968), an elastoplastic model for unsaturated soils was proposed by Alonso et al. (1990), named Barcelona Basic Model (BBM). That model accounted for large deformations, high deviatoric stresses and softening. The BBM reproduces most of the characteristic features of partially saturated soils, such as:

- An increase of shear strength and preconsolidation pressure  $p_0$  with suction.
- The development of reversible swelling strains when suction decreases at low confining stresses.
- The occurrence of irreversible collapse strains when suction decreases at high confining stress.
- The development of irreversible shrinkage when suction increases above a threshold value.

Later, Alonso et al. (1999) presented the Barcelona Expansive Model (BExM) to improve the modelled behaviour of highly expansive soils. It is based on the consideration of two levels of structure: a microstructural level (at which swelling of active minerals takes place, i.e. smectite) and a macrostructural level (for major structural rearrangement). The model adopts the following assumptions:

- The microstructural level is mainly saturated.
- The microstructural behaviour is elastic and volumetric.
- A mechanical, hydraulic, and chemical equilibrium exists between micro- and macro-structure.
- Coupling is considered between elastic microstructural strains and elastoplastic macrostructural strains.

This soil mechanics model has evolved to reproduce the free swelling behaviour of bentonite in the presence of voids or erosion processes. The formulation presented by Navarro et al. (2017) continues with the use of the double porosity model, adopting the BExM as the base stress-strain constitutive model and calculating macrostructural strains as in the BBM (with some non-linear elastic variations).

To incorporate the macrostructural strain induced by bentonite destructuration, a state surface is proposed by Navarro et al. (2016). The separation of particles and aggregates that causes these free swelling strains is properly characterised. This new state surface also includes swelling dependence on the salinity conditions. To account for large swelling strains, another modification is introduced to characterise the macro-porosity increase not included in the aggregates de-structuration.

As in this model salinity is not negligible, microstructural matric suction is differentiated from the matric suction of the macrostructure. The formulation presented in Karnland et al. (2005) is adapted by including a microstructural osmotic coefficient. Thus, the increase in microstructural suction due to the contribution to the chemical potential by ions in excess of the cation exchange capacity (Navarro et al. 2017).

This resulting model is capable of representing bentonite expansion under free swelling conditions from a soil mechanics point of view. It is based on a two-level porosity model, with non-linear constitutive equations and accounting for salinity effects in expansion.

## 2.2 Available experiments

In the last decades, numerous laboratory experiments have been achieved to characterise bentonite expansion and erosion. A large number of these experiments has been done within the framework of the BELBaR project in recent years.

These experiments can be classified by the process they are focused on. Following this classification, two groups are of interest to the present study: pure swelling tests and bentonite experiments where expansion and erosion are included.

The first group accounts for those experiments where there is no erosion. Some examples are:

- simulated oedometric tests (e.g. Sołowski and Gallipoli 2010),
- free swelling tube experiments, e.g. those carried out at B+TECH in Finland, at KTH by Dvinskikh et al. (2009), free swelling in a narrow channel by Harjupatana et al. (2015), and the tests from Liu et al. (2009a) using sodium montmorillonite,
- perforation hole tests.

In the second group, experiments are not only focused on bentonite expansion but also in its erosion characterisation:

- pinhole test simulation for swelling and mechanical erosion of an MX-80 bentonite (Sane et al. 2013),
- BELBaR benchmark, erosion processes under flowing water conditions, studied by Clay Technology AB, B+Tech Oy, and ÚJV Řež (BELBaR deliverable D2.8),
- laboratory studies on the extrusion and erosion behaviour of bentonite buffer material in artificial fracture systems (Schatz et al. 2013),
- swelling and erosion in artificial fractures, montmorillonite phase behaviour (Hedström et al. 2016).

From all these experiments, one of each group has been selected here for further analysis. They have been selected due to the bentonite used, the complete parametrisation and test setup included in the reports, and due to their simplicity. Avoiding geometric complexity or coupling of different effects helps to enhance the pure expanding and eroding process.

### 2.2.1 Free swelling experiment

Selected experiments were those presented by Sane et al. (2013). The aim of the analysis of these experiments is to calibrate the bentonite expansion model. Simple swelling in a transparent vertical cylindrical tube is tested. MX-80 bentonite blocks with a height of 40 mm and a diameter of 50 mm were compacted to 2.03 g/cm<sup>3</sup> of bulk density and with a 17 % water content. Averaged mass for blocks was 159.5 grams. For measurement purposes a sintered plate was placed over the block. Four types of groundwater simulants with salinities of 0 g/l (de-ionised water), 1 g/l, 10g/l, and 70 g/l were used. The experiment outputs are presented as vertical swelling displacement with time. The effect of salinity in swelling can be summarised by the following statement: an increase in salinity is followed by higher initial swelling rates and a faster stabilisation of swelling.

### 2.2.2 Swelling and erosion in an artificial fracture

For the erosion tests, the studied series of experiments was that presented by Schatz et al. (2013). This series of experiments, in which bentonite could swell and erode into a well-defined planar fracture, was performed to simulate the potential swelling and erosion behaviour of bentonite buffer material at a fracture interface. Starting materials were sodium and calcium MX-80 bentonites.

Bentonite samples were compacted into 20 × 20 mm cylindrical blocks with a dry density of 1.6 g/cm<sup>3</sup>. The experiments were carried out in an artificial fracture cell especially designed for that study. The cylindrical plug was confined in a centred section intersected in the middle by a horizontal flow path of known aperture. The general protocol for the tests began with the sample emplacement and system sealing, followed by the saturation of the samples and pumping flow

through the fracture. Many tests were performed with different bentonite compositions, salinity of the solution or flowing rates. The main findings were the relation between solution salinity and the occurrence or not of erosion, and its relation with extrusion distance.

### **2.3 Concluding remarks**

Bentonite behaviour under repository conditions is mainly characterised by two processes: extrusion/swelling and erosion. Both must be correctly characterised to assess the bentonite buffer stability in the long-term.

Currently available modelling approaches undertake this phenomenon from different perspectives. The use of a novel two-region model (Neretnieks et al. 2017) has led to reasonably good results through a dynamic diffusive model. Other models are based on classical soil mechanics, as the one presented in Navarro et al. (2017). It solves the swelling of bentonite through a non-linear constitutive model for bentonite with two porosity levels.

Experimental small-scale tests have been achieved with multiple procedures, many of them are related with the European project BELBaR. The simplest ones, those accounting for vertical free swelling (Sane et al. 2013) and bentonite erosion through an artificial fracture (Schatz et al. 2013) were selected in the present work. They are able to characterise the entire process, differentiating swelling from erosion implications. Solution salinity is an important factor in both processes.

The availability of experimental results for these two processes (swelling and erosion), and the conceptual separation in the modelling approach presented by Neretnieks et al. (2017) gives rise to the idea of conceptualizing these two regions from different points of view. The description of the flocculation process in the erosion region by the dynamic diffusive equation could be enriched by a description of the expanding region through a soil mechanics model for expanding clays (BExM).



## 3 Application of particle-based approach to the study of bentonite erosion

### 3.1 Continuum models

The work by Neretnieks et al. (2017) presents a numerical method that can be used to simulate the evolution of clay mass balance as this material expands into the fracture region, under the influence of the incoming water flow. Specifically, this work focusses on the clay contained in a flat fracture intersecting the cylindrical canister orthogonally to its axis. Given the small fracture aperture relative to the perimeter of the buffer, these authors give a purely two-dimensional description of the domain. The domain is defined as the region comprised between the canister perimeter, the two fracture walls and infinity. The medium is treated as a two-phase continuum with varying proportions of clay and water. The scalar field  $\varnothing(t,x,y) \in [0,1]$  stands for the solid fraction, relating the volume of clay particles with the total volume unit. Consequently, the fluid fraction (water ratio) is given by  $1-\varnothing$ . The determination of any of these two fields completely defines the state of the system.

In Neretnieks et al. (2017) work, the evolution of  $\varnothing$  is assumed to follow a (nonlinear) convection-diffusion equation, the nonlinearity is contained in the definition of the diffusivity function, as it depends on  $\varnothing$  and  $c$  (local ion concentration). This model assumes that the tendency of the clay to expand can be explained by the addition of two effects: diffusion of clay mass, acting in the entire domain and powered by the inter-particle forces; and mass advection of clay particles due to the incoming flow. In this model, the presence of the particles is coupled to the flow by the variation of kinematic viscosity value, which is also a function of  $\varnothing$ . In turn, it is involved in the calculation of  $D$ .

All the physical complexity is thus encoded in the diffusivity function,  $D(\varnothing,c)$ . However, given that  $c$  is assumed to be constant in the entire domain (it is a property of the incoming flow), and its variation is considered to be sudden (compared to the evolution of the system), it can be treated as a constant, yielding  $D = D(\varnothing)$ . The precise expression for  $D(\varnothing)$  can be found in the work by Liu et al. (2009a, b) and will be reproduced below.

It has been experimentally observed (Moreno et al. 2011, Neretnieks et al. 2017) that two distinct regions develop in this system. The first region is the inner region, comprised between the buffer perimeter out to a distance at which the solid fraction has fallen to certain (small) value  $\varnothing = \varnothing_R$ . This distance defines a perimeter, which has also been observed to be approximately circular and is, in fact, taken as such in Neretnieks et al. (2017). In this region, the clay behaves like a gel and does not flow under the viscous stresses of the incoming fluid, behaving as a porous medium with infinite viscosity. The second region, the outermost zone, is called the rim region and includes the space defined by the circular corona between  $\varnothing = \varnothing_R$  and  $\varnothing \approx 0$ . In this region, the medium behaves like a sol, and it flows like a fluid driven by the shear stresses produced by the seeping water current.

The distinction between these two regimes has motivated the use of a partitioned approach in Neretnieks et al. (2017). On the one hand, the rim region is described by a full convection-diffusive equation, although its thinness allows to make some additional geometric simplifications. On the other hand, the inner region is described by a pure diffusive equation, where its outer (mass flux type) boundary conditions are obtained from the solution in the rim region.

In the following paragraphs an overview is given of the corresponding transport equations as were used in Neretnieks et al. (2017).

#### 3.1.1 Mass conservation equation

In order to pose the mathematical problem coordinates  $x$  and  $y$  are defined, corresponding to the perimetric and normal directions respectively. Thanks to the small width of the rim zone, its curved area can be ‘unwound’ with negligible error onto a rectangular region of space, making  $x$  and  $y$  Cartesian coordinates. Direction  $x$  is bounded between zero and half the perimeter (that for which  $\varnothing = \varnothing_R$ ). This perimeter might indeed change as the clay flows from the buffer into the fracture,

but this expansion can be considered to be very slow compared with the time it takes the rim region system to reach a stationary solution (Neretnieks et al. 2017). It can thus be taken as a constant for the present discussion, defined as  $x \in \left[0, \frac{D_{buffer}}{2}\pi\right]$ .

On the other hand, only the far-field boundary conditions are known *a priori* in the radial direction, so  $y$  must be taken as  $y \in [0, \infty]$ . Although most of the variation in  $\phi$  is expected to occur in a very thin region compared to  $D_{buffer}$ , as mention before. This discussion is brought back in Section 3.2.1. The problem consists in finding a field:

$$\phi : I \times C_{rim} \rightarrow [0, 1]; (x, y) \rightarrow \phi(x, y) \quad (3-1)$$

with  $I = [0, T]$ , where  $T$  is the final time and  $C_{rim} = \left[0, \frac{D_{buffer}}{2}\pi\right] \times [0, \infty]$ , where  $D_{buffer}$  is the buffer diameter; such that:

$$\frac{\partial \phi}{\partial \tau} = \nabla \cdot (D(\phi)\nabla \phi) - \mathbf{u} \cdot \nabla \phi \text{ in } I \times C_{rim} \quad (3-2)$$

where  $\mathbf{u}$  is the local fluid velocity; with the following boundary conditions:

$$\left. \begin{aligned} \phi(t, x, 0) &= \phi_R \\ \phi(t, x, \infty) &= 0 \end{aligned} \right\} \forall t \in I, x \in \left[0, \frac{D_{buffer}}{2}\pi\right] \quad (3-3)$$

### 3.1.2 Diffusivity function

The diffusivity function was developed by Liu et al. (2009a, b) based on their analysis of the force between two clay particles held parallel at a distance  $h$ . A formula for the diffusivity was then obtained after assuming that: (1) the coin-shaped particles are identical and lay parallel to each other, (2) the distance  $h$  is the average distance between them and (3) hydrodynamic interactions between particles can be averaged by modifying the viscous friction coefficient with the Kozeny–Carman equation. Thus, reading:

$$D(h) = \frac{k_B T}{\xi} + \frac{(h + \delta_p)^2}{\xi} \left( \frac{\partial F_{vdW}}{\partial h} - \frac{\partial F_{DDL}}{\partial h} \right) \quad (3-4)$$

where  $\delta_p$  is the particles' thickness,  $F_{vdW}$  is the magnitude of the van der Waals force and  $F_{DDL}$  that of the diffuse double-layer force. The parameter  $\xi$  is the viscous friction coefficient, for the case of particles that are far apart can be expressed as (Liu et al. 2009a):

$$\xi = 6\pi\eta\omega C + V_p k_0 \tau^2 a_p^2 \eta_w \frac{\phi}{(1-\phi)^2} \quad (3-5)$$

where  $V_p$  is the volume of the particle,  $a_p$  is the specific surface area per unit volume of particles,  $k_0$  is the pore shape factor and  $\tau$  the tortuosity of the flow channels ( $k_0 \tau^2$  is Kozeny's constant);  $C$  is the equivalent capacitance of the particles ( $C = a$  for spherical particles, where  $a$  is the radius of the particle), which is given by:

$$C = \frac{\frac{\delta_p}{2} \sqrt{\frac{4S_p}{\pi\delta_p^2} - 1}}{\text{atan}\left(\sqrt{\frac{4S_p}{\pi\delta_p^2} - 1}\right)} \quad (3-6)$$

where  $S_p$  is the surface area of the particles. The force  $F_{vdW}$  is calculated according to the De Boer theory (Liu et al. 2009a) as:

$$F_{vdW} = \frac{A_H S_p}{6\pi} \left( \frac{1}{h^3} - \frac{2}{(h + \delta_p)^3} + \frac{1}{(h + 2\delta_p)^3} \right) \quad (3-7)$$

where  $A_H$  is the Hamaker constant. And the magnitude of the diffusive double-layer force is:

$$F_{DDL} = 2cRTS_p(\cosh(y^m) - 1) \quad (3-8)$$

where  $c$  is the electrolyte's concentration and  $R$  is the gas constant. Note that these are scalar definitions of the forces. This is due to the assumption of considering parallel plate-like particles and that the scalars are the magnitude of the (incoming) force vectors, that run along the orthogonal direction of the pair of particles under consideration.

Now, neglecting Stern-layer corrections, using the 'compression' approach and the Gouy–Chapman theory, see (Liu et al. 2009a), a good approximation of the midway potential is given by:

$$y^m = \sinh^{-1} \left( 2 \sinh(y_\infty^m) + \frac{4}{kh} \sinh \left( \frac{y_\infty^h}{2} \right) \right) \quad (3-9)$$

$$y_\infty^m = 4 \tanh^{-1} \left( \tanh \left( \frac{y_\infty^0}{4} \right) \exp \left( -\frac{kh}{2} \right) \right) \quad (3-10)$$

$$y_\infty^h = 4 \tanh^{-1} \left( \tanh \left( \frac{y_\infty^0}{4} \right) \exp(-kh) \right) \quad (3-11)$$

where  $\kappa$  is the reciprocal Debye length, given by:

$$k = \sqrt{\frac{2cF^2\omega^2}{\varepsilon_0\varepsilon_rRT}} \quad (3-12)$$

and the dimensionless surface potential of the isolated plate is:

$$y_\infty^0 = 2 \sinh^{-1} \left( \frac{\omega F \sigma^0}{2\varepsilon_0\varepsilon_r\kappa RT} \right) \quad (3-13)$$

where  $\omega$  is the valence of the counter-ion (not called  $z$  here to avoid a clash with the previously defined coordinate),  $F$  is the Faraday constant and  $\sigma^0$  is the surface charge density of the particle.

Finally, an expression for the relative viscosity of the suspension is given by (Liu 2011):

$$\eta r(\varphi_{\text{cov}}) = 1 + 1.022\varphi_{\text{cov}} + 1.358\varphi_{\text{cov}}^3 \quad (3-14)$$

$$\varphi_{\text{cov}} = \frac{2V_e d_p}{3 \delta_p} \varnothing \quad (3-15)$$

$$V_e = \left( 1 + \frac{2}{d_p} \frac{m}{k} \right)^3 \quad (3-16)$$

although, this expression is only valid for  $\varphi_{\text{cov}} < 1.6$ . For higher concentrations, the suspension stops flowing under the prevailing flow conditions (Neretnieks et al. 2017). Here,  $m$  is a numerical factor that relates the Debye length to the extent of the 'core' of the electric double layer from the particle's surface (Liu 2011).

Note that Equation 3-4 is written in terms of  $h$ , which is the average distance between particles. In order to write it in terms of the solid fraction it is necessary to make some assumption about the spatial ordering of the particles. In the works of Liu et al. (2009a, b) it is assumed that the particles are stacked on top of each other, with their flat surfaces all parallel to each other and negligible space between neighbour stacks. In this case:

$$\varnothing(h) = \frac{\delta_p}{\delta_p + h} \quad (3-17)$$

### 3.1.3 Results and known limitations of the continuum models

The theory presented above was tested with a set of experimental tests and the results were summarised in Neretnieks et al. (2017). The experiments consisted in forcing water to flow between two methacrylate plates placed parallel (separated one millimetre) to model the fracture walls. Trapped between the two walls a 2cm-diameter cylindrical piece of refined bentonite was placed, water flow and clay expansion and erosion rates were recorded. Several ionic concentrations and various types of bentonite were used in the experiment. The range of values considered for the flow rates and ion concentrations covered those expected in repository conditions.

The CCC point is the critical ionic concentration above which a stability point exists, is such that attractive van der Waals forces become stronger than the repulsive diffuse double-layer forces (that have a much faster asymptotic decay with particle separation). For low ionic concentrations, DDL forces decay is slower; thus, the separation at which they are overwhelmed by the van der Waals forces is greater. However, at this point, these forces have become so weak that they are not able to avoid the escape of particles due to Brownian motion, diffusing away without bound.

For cation concentrations above the CCC point, the clay expansion is expected to become stable and this behaviour is correctly reproduced by the model. The amount of expansion was reasonably predicted, although some discrepancies remained. Since in this regime there is no rim zone in the sense described above (clay continuously being eroded away by the incoming flow), the error must have been due to the inner zone model.

The most important discrepancies with the experiments were found for concentrations below de CCC point. For low ion concentrations, the clay expands unboundedly until the local solid fraction near the perimeter is so low that the gel-like properties are lost and the clay forms a sol. The solid fraction of the sol drops to almost zero in a thin region called the rim region, effectively turning into a fluid that is incapable of resisting the shear stresses from the incoming flow, which continuously erodes it. For this case, a clear tendency of the model to under-predict the clay erosion rate was reported. The error levels were variable but reached at least one order of magnitude in relative terms.

A single theory was presented by Neretnieks et al. (2017) to explain this inconsistency. It was based on the formation of clay agglomerates, which had not been anticipated, but were observed in the experiments. These flocs were visible to the naked eye and were observed to flow passively with water. The theory presented in Liu et al. (2009a, b) assumes a uniform suspension of clay particles prevalent throughout the rim region. In particular, the formulation of the modified viscosity is based on an experimental fit where no flocculation was observed (Liu 2011). Consequently, it becomes clear that if this flocculation occurs before  $\phi \approx 0$ , the model predicts an artificial slow-down of erosion with fluid velocity due to the increased local viscosity.

To take this effect into account in the model, the same authors propose to introduce a new critical solid fraction ( $\phi_{R,f}$ ), interpreted as the solid fraction at which flocculation takes place; assuming that, from that point on, the clay becomes a sol with the same viscosity as water. In other words, the transition takes place directly from a gel structure that does not flow, to a floc-laden water flow with the same viscosity as water. This conception is backed up by claiming that such transition was indeed observed to be as such, since: “the flocs did not slow down the water carrying the flocs as found by dye injection”.

By this approach, Neretnieks et al. (2017) were able to correct their results, obtaining good agreement with the experiments. Nonetheless, they acknowledged the unsatisfactory nature of this procedure, which may become invalid for different configurations than those studied in the experiments. They also recognised the need for further studies on the process of floc formation, which is poorly understood.

Indeed, it is thought that their insights are accurate and agree in the necessity of better understanding floc formation in order to predict the erosion rate with some reliability. Moreover, it is believed that this problem is ideally suited for study at the individual particle level. In Section 3.3 this technique is described and some application examples are shown; moreover, Section 3.6 discusses future developments with this technique for the study of flocculation.

### 3.1.4 Further critique

Studying the formulation presented in Neretnieks et al. (2017) work, some possible inconsistencies in the formulation were detected, these findings are summarised in Appendix A.

## 3.2 Analysis of scales

The physical system under study comprises a wide range of scales, which makes neither the micro or the macro approaches sufficient on their own. In this section, some estimates to determine the characteristic spatial and temporal scales of the problem are given. The goal is to gain an order-of-magnitude orientation of the system, this knowledge will be useful to assess the viability of different approaches.

### 3.2.1 Extent of rim zone

To estimate the length of the rim zone, the following equation describing the loss of bentonite at the rim zone is considered (Neretnieks et al. 2017):

$$\frac{\partial}{\partial y} \left( D\phi \frac{\partial \phi}{\partial y} \right) = \frac{u_0}{\eta_r} \frac{\partial \phi}{\partial x} \quad (3-18)$$

with the boundary conditions:

$$\begin{aligned} \phi &= 0 & \text{for} & & x &\leq 0 \\ \phi &= \phi_R & \text{at} & & y &= 0 \\ \phi &= 0 & \text{at} & & y &= \infty \end{aligned} \quad (3-19)$$

where  $x$  is the circumferential coordinate along the rim (its origin is placed at the point closest to where the flow comes from) and  $y$  is the radial direction (its origin is placed where the clay fraction starts to be deformed by the flow);  $u_0$  is the flow velocity magnitude; and  $\phi$  is the local solid fraction. Note that this simple formulation implicitly assumes that the extent of the rim zone is larger than the fracture separation ( $\delta_p$ ), which is of the same order as the viscous boundary layer that forms at the interface gel-sol. Otherwise, the rim region would be mostly inside the boundary layer and the assumption of a constant velocity that depends only on the local viscosity would break down.

By considering the change of variables:

$$z = \frac{y}{2\sqrt{D_0 \frac{x}{u_0}}} \quad (3-20)$$

The system defined by Equations 3-18 and 3-20 can be rewritten as:

$$D_r(\phi) \frac{d^2 \phi}{dz^2} + \frac{dD_r(\phi)}{d\phi} \left( \frac{d\phi}{dz} \right)^2 = \frac{-2z}{\eta_r(\phi)} \frac{d\phi}{dz} \quad (3-21)$$

with the boundary conditions:

$$\begin{aligned} \phi &= \phi_R \quad \text{at} \quad z = 0 \\ \phi &= 0 \quad \text{at} \quad z = \infty \end{aligned} \quad (3-22)$$

where:

$$\eta_r = \frac{\eta}{\eta_w} \quad (3-23)$$

$$D_r = \frac{D}{D_0} \quad (3-24)$$

being  $D_0$  is the thermal diffusivity in the absence of other inter-particle forces;  $\eta$  is the local viscosity and  $\eta_w$  is the suspending phase viscosity (without the particles). The different diffusivities can be calculated as (Liu et al. 2009a):

$$D_0 = \frac{k_B T}{\xi} \quad (3-25)$$

where  $k_B$  is Boltzmann's Constant and  $T$  is the absolute temperature.

Now, the extent of the rim zone is estimated, i.e. the thin region where the viscosity changes significantly as the gel turns into a sol that can be carried away by the incoming flow. For this estimation, Equation 3-21 is made non-dimensional, with all the relevant terms bounded of order one. Thus, allowing a direct comparison between the different terms (Krantz 2007). The rim zone will then be identified by requiring that the terms related to the inter-particle potentials cannot be neglected when compared to other effects such as the convection of particles by the passing flow.

Consider the following normalised counterparts of the independent and dependent variables:

$$z^* = \frac{z}{\delta_z}, \phi^* = \frac{\phi}{\phi_R}, D_r^* = \frac{D_r}{D_r(\phi_R)}, \eta_r^* = \frac{\eta_r}{\eta_r(\phi_R)} \quad (3-26)$$

where  $\phi_R = \phi(0)$  and  $\delta_z$  is the scale for which significant changes in  $\phi_R$  and, thus in  $D_r$  and  $\eta_r$  occur. In terms of these variables, Equation 3-21 reads:

$$\frac{D_r^*(\phi_R) \phi_R}{\delta_z^2} \left( D_r^*(\phi^*) \frac{d^2 \phi^*}{dz^{*2}} + \frac{dD_r^*(\phi^*)}{d\phi^*} \left( \frac{d\phi^*}{dz^*} \right)^2 \right) = \frac{-2\phi_R}{\eta_r(\phi_R) \eta_r^*(\phi^*)} \frac{z^*}{dz^*} \frac{d\phi^*}{dz^*} \quad (3-27)$$

with the modified boundary conditions:

$$\begin{aligned} \phi^* &= 1 \quad \text{at} \quad z^* = 0 \\ \phi^* &= 0 \quad \text{at} \quad z^* = \infty \end{aligned} \quad (3-28)$$

where the chain rule has been applied and the notation has been slightly abused by writing  $D_r^*(\phi^*)$  instead of  $D_r^*(\phi_R \phi^*)$  etc. Note that Equation 3-26 makes the normalised variables  $\phi^*$ ,  $D_r^*$  and  $\eta_r^*$  to be bounded between zero and one. This is because  $\phi_R$  is the maximum value of the porosity in the rim zone, while the other two variables are monotonic functions that grow with  $\phi$ . Note also that by using this scaling, the terms with first and second derivatives are guaranteed to be also of order one for a large proportion of the points. Specifically, the estimates:

$$\frac{d\phi^*}{dz^*} \sim \frac{\phi_R}{\delta_z}, \frac{d^2 \phi^*}{dz^{*2}} \sim \frac{\phi_R}{\delta_z^2} \quad (3-29)$$

become upper bounds for the values of the derivatives near  $z^* = \delta_z$ , where  $\delta_z$  is supposed to be of the order of the extent of the rim region. In other words, requiring that  $z$  is inside the rim becomes hard to fulfil only for points with actual derivatives expected to be significantly smaller than their

estimates in Equation 3-29. This means that these estimates can be safely assumed to be upper bounds in the calculation of the extent of the rim region. Now, dividing both sides of Equation 3-37 by the constant coefficient of the left-hand side and eliminating the asterisks to simplify the notation, the following equation is obtained:

$$\eta_r(\phi) \left( D_r(\phi) \frac{d^2 \phi}{dz^2} + \frac{dD_r(\phi)}{d\phi} \left( \frac{d\phi}{dz} \right)^2 \right) = - \frac{2\delta_z^2}{D_r(\phi_R)\eta_r(\phi_R)} z \frac{d\phi}{dz} \quad (3-30)$$

Note that both terms on the left-hand side are positive, thus, they must be balanced by the term on the right. Since the left side term is of order one by construction, the points outside the rim zone may be characterised by requiring:

$$\frac{2\delta_z^2}{D_r(\phi_R)\eta_r(\phi_R)} \gg 1 \quad (3-31)$$

which translates as:

$$\delta_z^2 = \left( \frac{\delta_{rim}}{\sqrt{D_0 \frac{x}{u_0}}} \right)^2 \gg \frac{D_r(\phi_R)\eta_r(\phi_R)}{2} \quad (3-32)$$

in the coordinates before the change of variables; where now  $\delta_{rim}$  is the length scale looked for. It is common to take  $A \gg B \Leftrightarrow A > 100B$  in practical applications. With this rule, and taking square roots at both sides of Equation 3-32, the following order of magnitude for the extent of the rim zone is obtained:

$$\delta_{rim}(x) \sim 10 \sqrt{\frac{x D(\phi_R) \eta_r(\phi_R)}{u_0}} \quad (3-33)$$

It is expected that most of the drop in fluid fraction (and thus in viscosity) takes place within the zone delimited by this variable.

Using some known ranges of the parameters involved to derive numerical orders of magnitude for  $\delta_{rim}$ ,  $R = 0.2$  is fixed, since this value is not expected to change sensibly. Similarly,  $\eta_r(\phi_R) = 40$ ,  $c = 0.1$  and  $\phi = 0.01$  are defined from Moreno et al. (2010). A suitable range for the different parameters is included in Table 3-1, along with a chosen representative value. The values in Table 3-1 result in a range of values for the extent of the rim zone of:

$$\delta_{rim}(x) \in (0,005\sqrt{x}, 0,5\sqrt{x}) \text{ [m]} \quad (3-34)$$

with a characteristic value of  $\delta_{rim}(x) \sim 0.01$  m.

**Table 3-1. Physical parameters considered in the cellular flow example.**

Parameter	Range	Characteristic value	Description
$x$	0–100 m *	0.01 m	Circumference of intrusion
$D(\phi_R)$	$1 \times 10^{-10}$ m <sup>2</sup> /s	$1 \times 10^{-10}$ m <sup>2</sup> /s	Max. diffusivity
$\eta_r(\phi_R)$	5–40 <sup>b</sup>	10	Max. relative viscosity
$u_0$	$5 \times 10^{-6} - 2 \times 10^{-4}$ m·s <sup>-1</sup> *	$1 \times 10^{-5}$ m·s <sup>-1</sup>	Characteristic velocity

\* Neretnieks et al. (2017); b: Moreno et al. (2011).

### 3.2.2 Time to steady-state

In order to estimate the computational resources that are required to simulate a small portion of the sol region with the discrete element model (DEM), it is important to be able to estimate, at least roughly, the amount of simulated time necessary to produce meaningful results. Since it is difficult to set up an initial configuration of particles that is close to the steady-state, it is easier to consider simplified initial conditions and hope to simulate the relaxation process towards steady-state. There are two obvious options:

1. Set up a lattice of particles such that the average distance between particles corresponds to a specific value of the diffusion (a way to reliably impose gradients in concentration is not currently available), define the maximum concentration  $\phi_R$  and wait for it to expand. Since it is not certain how thick should the layer of particles be, one could use the above estimation of the rim extent as a reference.

2. The other option is to start with no particles at all and let them flow into the domain from an inlet up to equilibrium.

In this work the second option is studied, mainly due to simplicity reasons. The question to answer is: how long should it take for the clay to fill up the domain until an equilibrium is reached. Implementation details of DEM and reason from the continuous formulation are not (for the moment) specifically described. First, a rough idea of the main scales involved is needed. A first estimate for necessary conditions in which the assumption that a steady-state has been reached is derived, as before, using simple scaling arguments. The non-stationary version of Equation 3-18 is considered:

$$\frac{\partial \phi}{\partial t} + \frac{u_0}{\eta_r} \frac{\partial \phi}{\partial x} - \frac{\partial}{\partial y} \left( D(\phi) \frac{\partial \phi}{\partial y} \right) = 0 \quad (3-35)$$

by again applying the transformation in Equation 3-20 and considering the same dimensional factors as in Equation 3-26, along with:

$$t^* = \frac{t}{T} \quad (3-36)$$

where  $T$  makes the normalised time be bounded of order one up to steady-state, the normalised equation is obtained:

$$\frac{\delta_z^2}{D_r(\phi_R)} \frac{4x}{u_0 T} \frac{d\phi^*}{dt^*} + \frac{2\delta_z^2}{D_r(\phi_R)\eta_r(\phi_R)} \frac{z^*}{\eta_r^*(\phi^*)} \frac{d\phi^*}{dz^*} - \left( D_r^*(\phi^*) \frac{d^2\phi^*}{dz^{*2}} + \frac{dD_r^*(\phi)}{d\phi^*} \left( \frac{d\phi^*}{dz^*} \right)^2 \right) = 0 \quad (3-37)$$

Close to steady-state, the transient term is small compared to the other two, so that the same arguments given above still hold (these other terms must still largely balance each other). Furthermore, within the rim region, the coefficient of the second term is bounded of order one, as required above. For the transient term to be neglectable, the assumption that its coefficient is much smaller than one is imposed:

$$\frac{\delta_z^2}{D_r(\phi_R)} \frac{4x}{u_0 T} \ll 1 \Rightarrow T \gg \frac{4\delta_{rim}^2}{D(\phi_R)} \quad (3-38)$$

which corresponds to a characteristic value of  $T \sim 10^6$  s (Table 3-1); i.e. in the order of a day.

## 3.3 Discrete element model

### 3.3.1 Basic Ingredients

Discrete Element Method algorithm fundamentals are here briefly reviewed. The goal is to introduce the relevant nomenclature and limit the scope of the discussion within this vast subject. A recent, widely, general review on the subject is presented in Guo and Curtis (2015).

The DEM consists in the numerical integration of the trajectories of a number of particles, which move according to Newton's laws under the action of both external forces, such as their own weight; and of contact forces, which act between particles when they become close enough. The numerical integration is typically calculated with a finite difference scheme, which in the great majority of implementations is explicit in nature. The reason for this has been discussed in the literature (Samiei et al. 2013), the consensus is that the cost of an implicit implementation would be greater or, at least, would not justify the greater complexity and difficulty of implementation associated with it. Note, however, that our system is quite peculiar, so part of the arguments in this respect could break down in this case. Section 3-6 presents further comments on this issue.

In the simplest versions of the method, each particle is modelled as a rigid sphere, and its (rigid solid) movement is determined by the position of its centre and its angular velocity vector, both of which evolved in time by the integration scheme. The presence of bounding walls can in turn be modelled by a set of flat rigid faces. For instance, in our implementation, the bounding surfaces are triangulated in the pre-process step, so that each resulting triangle defines a rigid face.

The most popular variety of the DEM is the soft-sphere method. In this version the particles are allowed to overlap (slightly) over each other and also penetrate the walls. Any given overlap is characterised by a point inside the overlapped region (the contact point). Its magnitude is represented by a scalar  $h$  (the indentation or penetration), which measures how far into each neighbour the contact point has moved. Associated with it there is a contact force and, sometimes, also a contact moment, which are added to the total actions being applied to the particle. These contact forces and moments

are typically functions of  $h$  and its derivatives, and sometimes of their histories too. The simplest versions include a linear spring and dash-pot rheological model, which depend linearly on  $h$  and  $\dot{h}$ . Although the contact model can become much more complicated, often devised with a particular application in mind. Normally, a number of free parameters allow to calibrate these micro-scale models by comparing the resulting macroscopic motion with experimental results.

In order to avoid the  $O(N^2)$  (where  $N$  is the number of particles plus walls) brute-force check of all the possible overlaps, a suitable search algorithm is always used to determine the correspondence between each particle and its neighbours. State-of-the-art algorithms achieve  $O(N \log N)$  scaling or even  $O(N)$  (Williams et al. 2004).

To summarise, Figure 3-1 presents the typical DEM.

### 3.3.2 Equation of motion for the particles

The theory that underlies the work by Krantz (2007) and in fact the model used by Neretnieks et al. (2017) is the same theory that can be used to describe the motion of the particles. It is a matter of stopping the argument before the upscaling step that allows the derivation of the diffusivity. The relevant equation is written down as:

$$mp \frac{d\mathbf{w}}{dt} = -\xi \mathbf{w} + \mathbf{F}_{wdw} + \mathbf{F}_{DDL} \quad (3-39)$$

where  $\mathbf{w}$  is the slip velocity, the first term on the right-hand side is the steady drag force and the other two terms are the vector counterparts of  $F_{vdw}$  and  $F_{DDL}$ , obtained by linear combination of the forces coming from all the neighbouring particles. Equation 3-39 involves a number of implicit assumptions; some of these assumptions might potentially lead to weaknesses in the theory, thus, they are discussed at this point.

#### First assumption: Steady drag

Equation 3-39 can be viewed as a restricted version of the Maxey–Riley equation (MRE) (Maxey and Riley 1983), with a modified friction coefficient to take into account the presence of other particles in an averaged way. This equation is valid for an isolated particle at very small particle Reynolds numbers, i.e.:

$$Re_p := \frac{a \|\mathbf{w}\|}{\nu} \ll 1 \quad (3-40)$$

---

1: $t \leftarrow 0.0$	➤ time
2: $n_{\text{step}} \leftarrow 0$	➤ time step
3: InitializeParticles()	➤ Create particles and initial conditions
4: SearchNeighbours()	
5: <b>while</b> $t < \text{FinalTime}$ <b>do</b>	
6: $t \leftarrow t + \Delta t$	
7: $n_{\text{step}} \leftarrow n_{\text{step}} + 1$	
8: <b>if</b> $\text{mod}(N_{\text{Search}}, n_{\text{step}}) == 0$ <b>then</b>	➤ search every $N_{\text{Search}}$ integration steps
9:         SearchNeighbours()	➤ assign neighbour elements to each particle
10: <b>for</b> $i = 1, \dots, N_{\text{Particles}}$ <b>do</b>	➤ for each particle
11: $f_i \leftarrow 0.0$	➤ total force for particle $i$
12: $f_i \leftarrow f_i + \text{CalculateExternalForces}(r_i, v_i)$	➤ e.g. gravity
13: <b>for</b> $k_{\text{neigh}, i} = 1, \dots, n_{\text{neigh}, i}$ <b>do</b>	➤ for each neighbour
14: $f_i \leftarrow f_i$	➤ from current overlap and its derivative
+CalculateContactForce( $r_i, v_i, r_k, v_k$ )	
15: <b>for</b> $i = 1, \dots, N_{\text{Particles}}$ <b>do</b>	➤ for each particle
16: $r_i, v_i \leftarrow \text{UpdatePosition}(r_i, v_i)$	

---

**Figure 3-1.** Typical DEM algorithm.

where  $\nu$  is the kinematic viscosity of the surrounding fluid. The theory makes use of the linear Stokes flow to derive the hydrodynamic forces on a submerged sphere, which explains the need for requiring Equation 3-40. The MRE contains a number of terms, all of which except the steady drag force and the buoyancy term (Archimedean displacement force plus weight) vanish if  $\mathbf{w}$  is constant. In Equation 3-40 these terms (along with the buoyancy, for simplicity) have been neglected, implying that the derivative of  $\mathbf{w}$  is very small most of the time. This is acceptable when the particle spends most of its time with a velocity very close to its terminal velocity. Section 3.3.3 shows that this hypothesis is acceptable for the current system, in which the particles accelerate extremely fast. This assumption is shared with the model of Neretnieks et al. (2017).

### Second assumption: Single particle theory

The MRE assumes the single-particle theory, meaning that hydrodynamic interactions between neighbouring particles are neglected. Thus, the expression for the friction drag is modified to consider the collective effect of many particles by the so-called Kozeny–Carman model (LeVeque 2008). Such effect is an upscaled scheme and does not take into account individual effects. The Kozeny–Carman model is normally applied to soils (porous media), in these the distances between particles are typically much smaller and it is reasonable to assume that the particles are static. Such assumption might become quite strong in the context of a dilute sol, where the particles are free to rotate and respond to the inter-particles potentials and the flow.

On the other hand, it is well known that the leading-order pair-wise interactions decay is inversely proportional to the distance between particles (Durlafsky and Brady 1989). As a consequence, these contributions are potentially important up to distances of several radius. It is important to realise that although the solid fractions in the present applications are quite dilute  $\phi \in (0.001, 0.01)$ , the corresponding distances turn out to be not that small as a result of their extreme shape. Indeed, the average separation,  $\bar{h}$ , can be calculated from:

$$\bar{h} = \left( \frac{V_p}{\phi} \right)^{1/3} \quad (3-41)$$

where the particle's volume  $V_p$  can be estimated as if its shape was a circular cylinder as:

$$V_p \sim \pi a^2 \delta_p \quad (3-42)$$

where  $\delta_p$  is the particles thickness and  $a$  its radius. The typical sizes cited in Neretnieks et al. (2017) yield (i.e. for  $a \sim 10^{-7}$ ,  $\delta_p \sim 10^{-9}$ ,  $\phi \sim 10^{-3}$ ):

$$\bar{h} \sim 10^{-7} \text{ [m]} \quad (3-43)$$

Note that this expression is not consistent with the work by Schatz et al. (2013). However, the arrangement assumed does not correspond to what is obtained when using spheres. The difference between both approaches is shown in Figure 3-2. It is not clear that their effect can be reduced to the upscaled Kozeny–Carman model, the issue deserves further study.

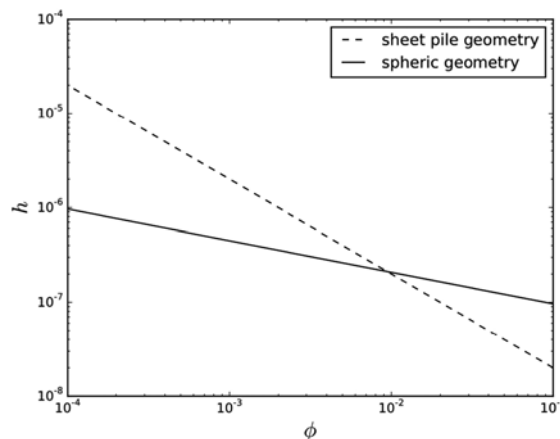


**Figure 3-2.** Average distance between particles as a function of the solid fraction. Two different geometrical configurations are compared: a sheet pile arrangement, where the flat particles tend to stack on top of each other, and a regular cubic lattice formed by spheres.

### Third assumption: spherical particles

The extremely flattened shaped of the typical clay particle has been already mentioned. Even though the hydrodynamic disturbance that the particle produces around it and the diffuse double layer field that tends to 'round up' the flat shape, it is still likely that this assumption introduces a considerable error.

First, such assumption breaks the anisotropy that is expected in the expanding clay and that is in fact assumed in the derivation of the diffusivity in (Liu et al. 2009a), where the particles are assumed to pile up in stacks, parallel to one another. Secondly, any effects considering particle rotation are lost. It is not clear how these effects would impact the expansion dynamics, but they surely would play a role in the formation of agglomerates, which has been identified as the main source of error of the formulation. Furthermore, macroscopic formulation of Neretnieks et al. (2017) also implies isotropy, since their diffusivity function is scalar.

However, the use of spherical particles introduces an additional difference since the packing configuration is cubic instead of the layered packing assumed in Liu et al. (2009a). Clearly, this aspect requires further study. Particles have been taken as spherical because no 'facet' or coin-shaped elements are currently implemented in Swimming DEM Application, of Kratos Multiphysics (Dadvand et al. 2010). The possibility of going on with such development is discussed in Section 3-6.

### 3.3.3 Contact model

The implementation of Equation 3-39 naturally fits into the contact model concept if a ball that contains the particle and extends out up to some cut-off distance is defined. This distance is such as the interaction fields become so weak that they can be safely be assumed to vanish. In this way, the role of the DEM particle is played by this ball and the role of the contact law is played by the van der Waals and diffuse double layer forces. Figure 3-3 shows the different radius defined for each particle. The cut-off radius ( $R_c$ ), defines the surface of the DEM particle, while the search radius ( $R_s$ ), is used to construct the lists of neighbours.

For a given set of physical parameters, the diffuse double-layer and van der Waals forces can be seen as functions of the separation  $h$  between particles, considering the cation concentration  $c$  as an additional given (although it can be made to depend on time) parameter. Or, equivalently, a function of the indentation, i.e.  $R_{c,1} + R_{c,1} - h_1 - h_2$  (the sub-indices identify the particles), conforming to the DEM basic model.

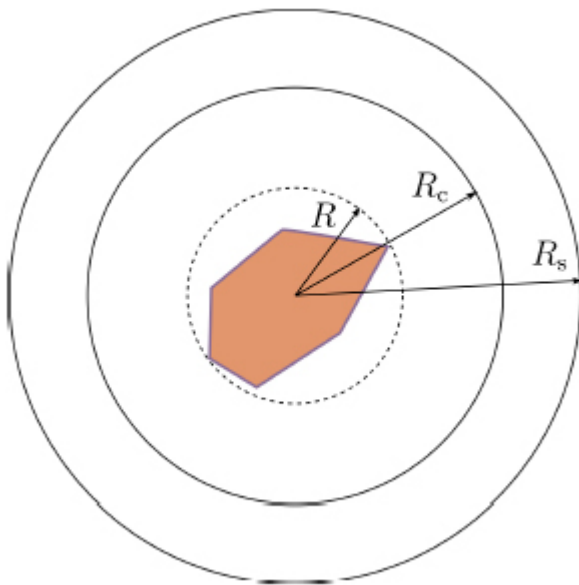


**Figure 3-3.** Radius hierarchy in the DEM model. Particles closer than the sum of their respective search radius ( $R_s$ ) are identified as neighbours. Forces only start developing after the balls defined by the cut-off radius ( $R_c$ ) overlap. The actual radius  $R$  of the idealised particle is only used to calculate physical properties of the particle, such as their surface area.

### 3.3.4 Time integration scheme

According to the standard DEM and Section 3.3.2, the equation of motion to be solved for any given particle should be:

$$m_p \frac{dv}{dt} = -\xi(v - u) + \sum_{i \in N} F_{wdW,i} + F_{DDL,i} \quad (3-44)$$

where  $\mathbf{v}$  is the velocity of the particle,  $\mathbf{u}$  is the velocity of the background fluid (already assumed to be quasi-stationary) and  $N$  is the set of the neighbouring particles' indices. Both the velocities and the forces depend on the distance  $h$ , while the friction coefficient  $\xi$  depends on a spatially averaged volume fraction. This volume fraction could be calculated by calculating the number of particles in a volume around the particle of interest, but is considered (at the moment) fixed for the sake of simplicity.

However, the particles' masses are extremely small, making the numerical solution of Equation 3-44 non-practical. Instead, the inertial term on the LHS are altogether neglected, assuming the hypothesis that the particles are always moving at their terminal velocity. Such approximation is justified by comparing the characteristic time scales associated with the unsteady motion with those associated to the steady motion of the particles.

For that, on the one hand, the relaxation time of the particle ( $\tau_r$ ), which is the time it takes for a particle to go, is considered to be  $1 - 1/e \approx 0.62$  times its initial velocity relative to the background fluid. On the other hand,  $\tau_t$  is considered to be the time it takes for a particle to travel, at its terminal speed, a distance equivalent to its own radius driven by a characteristic force is called. The magnitude of the characteristic force may be taken as the maximum repulsion force experimented by the particles at the highest solid fractions ( $\phi_R$ ). Then a measure of the importance of the unsteady effects can be presented as:

$$St = \frac{\tau_r}{\tau_t} \quad (3-45)$$

Referring to the characteristic values of Table 3-1, the following is obtained:

$$St = \frac{\frac{2a^2}{9v}}{\frac{1}{\xi} F_{DDL}(h(\phi_R))} = \frac{2aF_{DDL}}{9v\xi} \sim \frac{2 \cdot 10^{-7} \cdot 10^{-10}}{9 \cdot 10^{-6} \cdot 10^{-8}} \sim 10^{-4} \quad (3-46)$$

*terminal velocity*

And the scales are well separated, so the steady-state assumption is expected to be very accurate. Equation 3-46 allows to consider the alternative equation:

$$\dot{x} = u + \frac{1}{\xi} (\sum_{i \in N} F_{wdW,i} + F_{DDL,i}) \quad (3-47)$$

where  $\mathbf{v} = \dot{\mathbf{x}}$  is used, being  $\mathbf{x}$  the particle's position vector. Note that the equation of motion is now a first order equation, rather than a second order one. To solve Equation 3-47 (together with a suitable initial condition  $\mathbf{x}(0) = \mathbf{x}_0$ ), a finite difference scheme can be used. Several options are possible, here a version of the two-step Adams–Bashforth scheme has been used, given the limited level accuracy required and the need for good performance. The difference Equations read:

$$\begin{aligned} x_{n+1} &= x_n + \frac{\Delta t}{2} (3v_n - v_{n-1}) \\ v_{n+1} &= \frac{1}{2\xi} (3F_{n+1} - F_n) \end{aligned} \quad (3-48)$$

where:

$$F_n = \sum_{i \in N} F_{wdW,i}(h(x_n)) + F_{DDL,i}(h(x_n)) \quad (3-49)$$

This two-step scheme can be started with the analogue, first step version of the same algorithm.

#### Time Step

The selection of a suitable time step is crucially important in any DEM simulation, since it has a proportional impact in the numerical cost of the simulations. As in any finite difference calculation the selection of the time step is based on the required accuracy, so as to minimise the total number of time steps.

However, the choice is also restricted by the need to preserve numerical stability, which is always conditional to the size of the time step. In order to have an order-of-magnitude estimate of the time step size needed, to reason about the potential size of the numerical simulations, the maximum time step that will be allowable is calculated. For simplicity, the one-step version of the algorithm in an idealised situation is considered. This estimate is probably not far from the actual critical time step, even if a different scheme is chosen.

The motion of a particle, centred at an equidistant point between two other identical particles, is considered to be fixed. It is considered that the three particles are aligned on the  $x$ -axis, and that the origin is at the centre of the middle particle. Thus, the distance between the two extremal particles corresponds to twice the mean distance expected at the highest expected volume fractions (i.e.  $\varphi_R \sim 0.01$  for the current work). Such distance can be estimated (Figure 3-2) as  $1 \times 10^{-7}$  m. A cation concentration of  $c = 0.01$  of sodium-based bentonite is considered, being characteristic of the lower ionic strengths to be studied. It is assumed that the central particle is subjected to no other actions than the drag force and the forces  $F_{DDL}$  exerted by the other two particles (the van der Waals forces can be neglected with such low ionic strength).

Its equation of motion can then be simplified to the one-dimensional expression:

$$\dot{x} = \frac{1}{\xi} (F_{DDL}(h_0 + x) - F_{DDL}(h_0 - x)) \quad (3-50)$$

where it has been assumed  $h_0 = 1 \times 10^{-7}$  m. The discretised version of Equation 3-50 reads:

$$x_{n+1} = x_n + \frac{\Delta t}{\xi} (F_{DDL}(h_0 + x_n) - F_{DDL}(h_0 - x_n)) \quad (3-51)$$

The expression of  $F_{DDL}(h)$  is nonlinear and quite complicated. However, the stability of a linearised version of this equation can be studied. This is considered to give a good indication of how the nonlinear system will behave (LeVeque 2008). Thus, the following equation must be considered instead:

$$\dot{x} = \frac{1}{\xi} \left. \frac{dF(x)}{dx} \right|_{x=0} \quad X = \frac{2}{\xi} \left. \frac{dF_{DDL}(h_0+x)}{dx} \right|_{x=0} \quad x = \lambda x \quad (3-52)$$

since:

$$F(x) := F_{DDL}(h_0 + x_n) - F_{DDL}(h_0 - x_n) \quad (3-53)$$

makes sense in particular for small perturbations around the equilibrium point  $x = 0$ .

It is well-known that the discretised version of Equation 3-52 with the one-step scheme (forward Euler) yields a critical time step equal to (note that  $\lambda < 0$ ):

$$\Delta t_{crit} = \frac{2}{|\lambda|} \quad (3-54)$$

which also coincides with the characteristic time scale of the linearised system. Substituting the same characteristic values as before, it is found that  $\Delta t_{crit} \sim 10^{-5}$  s.

A sample simulation that confirms this estimate for the nonlinear system has been run. The central particle was initially perturbed to a position that deviated by  $0.1h_0$  from the equilibrium position and then left to evolve freely. Note that Section 3.4.1 shows that indeed the order of magnitude of the motion time is close to  $10^{-5}$  s. This means that any reasonable scheme should at least use a time step below this number to properly capture the evolution of the system. In Figure 3-4b the accuracy is almost totally destroyed, although the equilibrium point is eventually reached. For  $\Delta t = 10^{-5}$  s, the solution diverged.

In any case, it has become clear that the DEM method will require time steps below the  $10^{-5}$  s mark. This number should be useful in estimating how large a simulation is possible in practice.

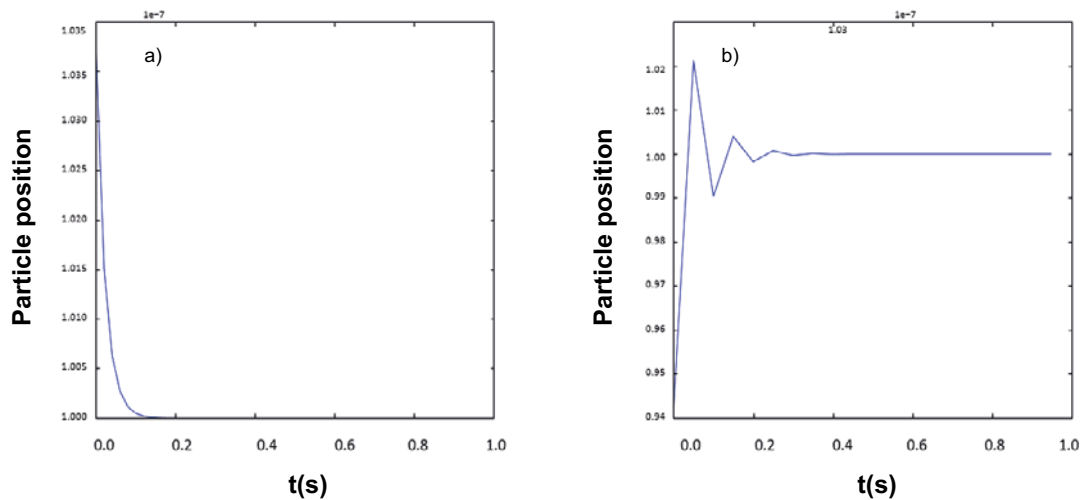


**Figure 3-4.** Evolution of particle position, calculated with the forward Euler method with  $\Delta t = 2 \times 10^{-6} \text{ s}$  (a) and  $\Delta t = 5 \times 10^{-6} \text{ s}$  (b).

### 3.4 Direct approach

In this section the possibility of applying the DEM to directly measure the variables of interest as a substitute of the continuum-based method is explored. As it is impossible to simulate the complete domain with all the particles involved.

Nonetheless, a relevant portion of this domain has been modelled, a thin parallelepipedal section of the rim region has been chosen. While a system that can output the macroscopic clay erosion rate is not able to be obtained, a set of tools and insights in this direction have been developed, they are summarised in this section. The new tools reported are related to the boundary conditions and particle tracking. Some estimates to illustrate the difficulties associated with the approach are also made and a few simulations that make use of them are discussed. All the developments have been implemented into the Swimming DEM Application of Kratos Multiphysics (Dadvand et al. 2010).

#### 3.4.1 Boundary conditions

The specification of adequate boundary conditions is certainly one of the most challenging tasks in this approach. For instance, in the continuum-based model described in the preceding section, it is perfectly possible to specify the solid fraction at a boundary while leaving its gradient untouched, or the other way around. With DEM, it is not as easy to decouple the two concepts. One problem is that the particles are introduced one by one, while the values that are wanted to be impose are actually averaged quantities over many particles (Section 3.5), these can only be known with precision after the particles have already been introduced. Also, it becomes problematic to apply a very strict input rate at a specific point, since this could lead to local excessive overlaps and make the simulation unstable. In this section the basic types of boundary conditions that have been considered are described and also how they can be realised in the context of DEM.

#### Wall conditions

This type of conditions is analogous to the null-normal-mass-flow continuum conditions. They can be realised by considering discrete face elements, which contact with the particles and apply a force of the same type as the inter-particle forces. Since these forces depend on the distance, it is only necessary to replace the distance between centres by the centre-wall distance. These elements are based on the triangulation of the geometric surfaces that form the boundaries. When these surfaces are flat, a very small number of triangles can be used, which makes their inclusion computationally affordable.

Based on this condition, a variant condition has been developed, instead of interacting with the particles it records all the particles that pass through it. With this tool, the mass flux through a user-defined surface can be tracked. In Figure 3-5 there is an example of such a surface, formed by two triangles (although those are not visible). Each triangle tracks the particles passing through them and the accumulated flux is recorded. This allows to produce plots such as the one in Figure 3-6, which corresponds to the sequence in Figure 3-5.

### Periodic conditions

These conditions can be applied to box-shaped domains. They imply the same conditions at the boundaries at a given side, as that at its opposite side. In order to realise these conditions with the DEM, it is necessary to adapt the search algorithm and the force calculation routines, so that a particle that is leaving the domain through one side is simultaneously entering it through the opposite one. Note that this is a stronger version of the periodic conditions than the continuum version, since here we are requiring the strict equality particle by particle, while in the continuous analogue, it would only be the averaged values that are required to coincide.

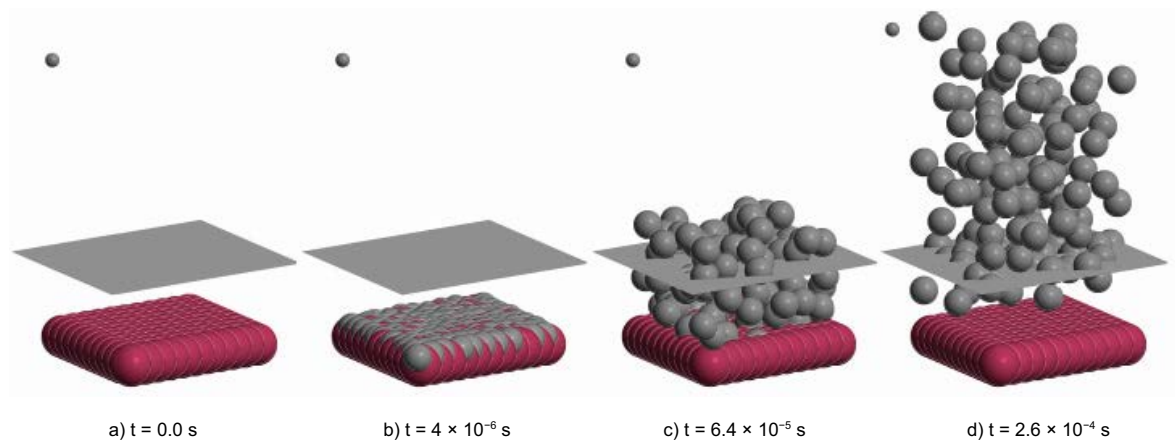


**Figure 3-5.** Sequence of captions from a simulation with a force inlet and a flux-measuring surface. The particles enter the domain very fast at first, but slow down as more and more particles pile up, blocking the inlet. A smaller particle was initially placed inside the domain to show two compatible ways to input particles. The injector 'egg' particles are depicted in red, while the measuring surface in grey.

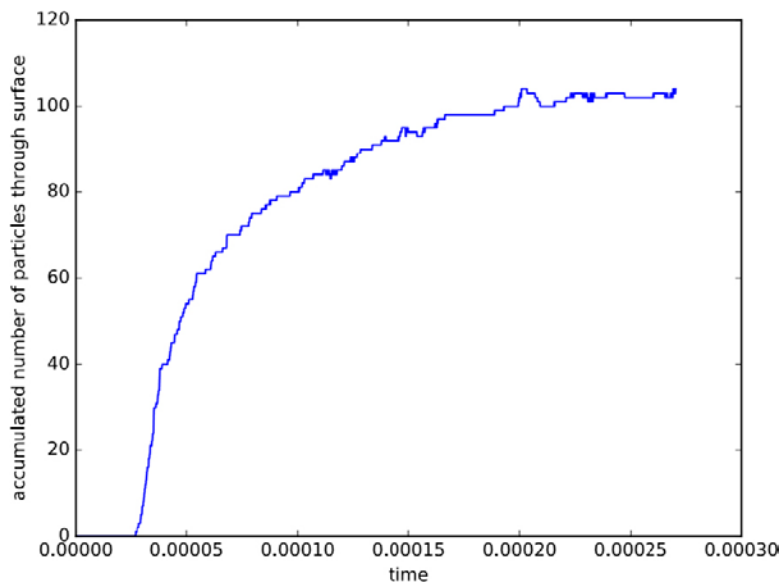


**Figure 3-6.** Number of particles passing through the analytic surface in Figure 3-5 in time.

This kind of boundary condition is adequate in long, cylindrical fluxes where the conditions do not change significantly along a distance of the order of the domain side length (the periodicity would then only apply along the direction of the flow). The alternative is to use flat wall conditions on either side of the domain, but of course this introduces a boundary effect, that should not be present with periodic boundaries. These boundary conditions could be used to represent a section of the rim region as long as there is no flow, as the development of the rim boundary layer breaks the symmetry between the two opposite sides of the domain that lay orthogonal to the flow.

While the capacity of particles to cross from one side to the opposite one was present previously in Kratos\_Multiphysics, more operations of search and force computations through the periodic boundary had to be implemented.

### **Imposed velocity conditions**

They consist in the injection of new particles through specified surface at a number of points of them. Their injection velocity is fixed until they are fully inside the domain, although it can be randomly selected from a spatial and temporal distribution. The typical direction of the velocity is chosen orthogonal to the surface, but it can also be perturbed by random orthogonal components to generate a more chaotic flow.

Note that if the continuum unknown is the solid fraction  $\phi$ , these conditions are analogous to the Neumann type or flux condition. As they specify the solid-fraction mass flow, being a result of combining the injection points spacings with the injection velocity. Note that these conditions can easily become incompatible with the particles already in the domain.

### **Imposed force conditions**

This type of conditions is like the imposed velocity ones, except that instead of imposing a velocity on the newly injected particles, it is a force that is imposed. If the newly injected particles find no neighbours around, their injection rate will be high. Instead, if there are many, closely packed particles in the domain, the injecting force might struggle to squeeze a new particle into the system.

Since the inter-particle force can be expressed as a function of the average particle spacing in the continuum description of the system, this type of conditions is actually related to the Dirichlet boundary conditions of the continuum description. The average injecting force can at first be fixed based in a few assumptions (particles' spacing and mean force per unit area). However, it is also possible to calibrate this force by adding the total force on each particle that is being injected during the simulation and comparing it to the expected macroscopic force (as derived from the value of  $\phi$  that it is intended to have fixed).

## **3.4.2 Computational cost**

DEM is computationally expensive. The reason for such statement (in most cases) lies on the very nature of the method, which attempts to resolve physical phenomena at two different time and length scales simultaneously. The micro-scale is defined by the contact dynamics between particles, which must be solved by the time discretisation scheme. On the other hand, the macro scales of interest are much bigger than the particle radius and have much larger characteristic time scales. The result is expensive simulations, involving many particles and time steps.

The computational cost of a DEM simulation can normally be divided into contributions mainly coming from: (1) neighbour search operations, to determine which particles overlap with which other particles; (2) contact forces calculations, to determine the contributions to the RHS of the equation of movement from each of the neighbours; and (3) particle kinematics updates, which involve updating the position and orientation of each particle according to the time integration scheme at every time step, including the necessary transformations to the local reference systems involved and the update of stored kinematics-related variables. Normally, contribution 3 is considerably smaller than the others.

Moreover, the computational cost due to the neighbour search algorithm has been identified as the dominant one among contributions 1 and 2 in DEM simulations in the past (Williams and O'Connor 1995). However, it is not expected this to be the case in practice, due to the following reasons:

- a. Our use of spheres, which greatly simplify the search operations.
- b. The cost of the force calculation-related operations (once the neighbours have been assigned), which can become quite high in practical realistic applications due to the use of relatively complex models with a significant number of variables to be set and stored during the simulation. The share of costs attributed to these operations is, for this reason alone, most often significant.
- c. The fact that search can be performed with a lower frequency than the time-integration, provided that an enlarged search radius is used. The search radius is the distance from a particle centre under which other particles are considered neighbours. If it the search radius is big enough there will be time to identify new neighbours before they collide, even if the search is performed every several time-integration steps, since the particles do not have time to become close enough before a new search step is performed. An optimal search radius is expected to exist for a given application. Indeed, a very big search radius would allow for very infrequent search, although many more neighbours would potentially be assigned to each particle, possible increasing the memory demands to unacceptable levels. On the other hand, a very tight search radius (it should always exceed the particle actual radius) would require more frequent search to avoid undesired initial large penetrations, leading to low accuracy and potential instabilities. Performing a search step at every step could damage efficiency dramatically. This possibility has been often ignored in the literature (Williams and O'Connor 1995).

And so, the cost is actually dominated by the force calculation operations, at least for reasonable-size problems that can be run on a PC. With the above considerations in mind, the overall computational cost of a DEM simulation is expected to depend mostly on:

1. the total number of particles ( $N$ ),
2. the cost per particle-time step ( $\Delta t_{PPTS}$ ),
3. the total number of time steps in the simulation ( $N_{\Delta t}$ ).

The most optimistic estimates would predict  $\Delta t_{PPTS}$  to remain constant as  $N$  grows. The cost per particle increases for large  $N$ , due to the larger data structures and higher chance of cache misses, for example. Nonetheless, this assumption suffices for the present discussion. Using the assumption that the cost due to force operations dominates the cost due to search as has been discussed, allows to produce the following estimate for the overall cost of a DEM simulation:

$$\Delta t_{wc} = NN_{\Delta t}\Delta t_{PPTS} \Rightarrow N = \frac{\Delta t_{wc}}{N_{\Delta t}\Delta t_{PPTS}} \quad (3-55)$$

where  $\Delta t_{PPTS}$  will strongly depend on the system regime, implementation and architecture.

Nonetheless, some preliminary calculations of what a single, modern, single-core PC could simulate in terms of the maximum number of particles and physical domain are done based on Equation 3-55.

For the simulation total duration, the estimate presented in Section 3.2.2 (i.e.  $\Delta t_{total} = 1 \times 10^6$  s) is used. On the other hand, the time step used for the numerical integration must be sufficiently small to both ensure adequate accuracy and avoid numerical instabilities. According to Section 3.3.4, a reference value of  $\Delta t \sim 1 \times 10^{-5}$  s is taken. Combining both estimates gives:

$$N_{\Delta t} \sim 10^{11} \quad (3-56)$$

Considering a state-of-the-art value for  $\Delta t_{PPTS}$  (i.e.  $1 \times 10^{-6}$  s) for general DEM simulations (Spellings et al. 2017). The number of particles that can be taken into account in a one-day calculation is:

$$N \sim \frac{3600 \cdot 24}{10^{11} \cdot 10^{-6}} \sim 1 \quad (3-57)$$

So only about one particle could be simulated for such a long simulation time in a single PC. The reason of course is the extremely large number of time steps needed to complete a full simulation, where the domain has been assumed to be initially empty and where the particles are injected until a macroscopically stationary boundary layer of clay-sol is fully formed. In other words: simulating the whole process is out of our reach.

In Figure 3-7 the evolution of the rim region developing from the interface at which  $\varphi \sim \varphi_R$  is shown. The vertical sides of the domain are periodic, this means that the development of the rim cannot have a stationary extent in this case (it corresponds to a point on an infinitely large clay buffer). Figure 3-7 also shows how slow its development becomes after only a small length of it has developed. Similarly, Figure 3-8 shows the expansion of clay being injected into an initially prepared cube of particles. After several hours of simulation, only a small compression front has developed on the bottom side.

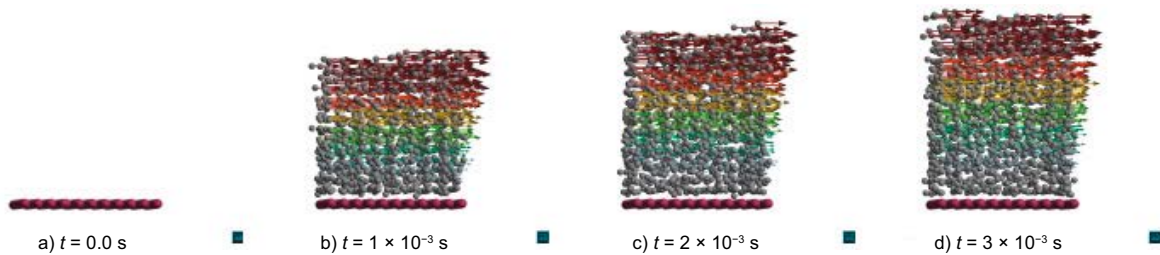


**Figure 3-7.** Sequence of captions from a simulation with a force inlet, periodic boundary conditions and an artificially imposed fluid flux that adapts to the particles' position. The profile is always exponential, with the lowest and highest values corresponding to the expected values reported in Neretnieks et al. (2017). The entire simulation took more than one day on a state-of-the-art PC. The arrows represent the fluid velocity, with the darkest colours corresponding to  $1 \times 10^{-4} \text{ ms}^{-1}$ . Around 2000 spheres are included in (d).

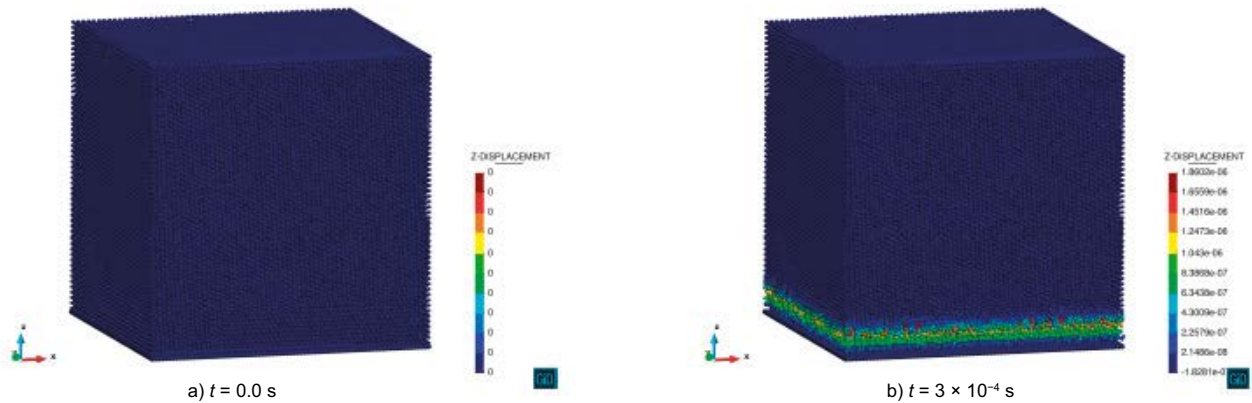


**Figure 3-8.** Sequence of captions from a simulation with a force inlet, periodic boundary conditions and with a still background fluid. The initial conditions included 370 000 particles, placed at an average distance of  $3 \times 10^{-7} \text{ m}$ . The time elapsed between both figures was several hours.

### 3.5 Recovering the macroscopic diffusivity

Given the large costs associated with the extreme ranges of spatial and temporal scales of the current problem, it is worth to consider an intermediate approach that might be computationally more manageable. It consists in running a relatively short transient simulation to estimate the value of the macroscopic diffusivity, as a function of the solid fraction (i.e.  $D(\phi)$ ), in which the physical model is encoded. By this technique, the values predicted by the formulation by Liu (2011) and Liu et al. (2009a, b) are expected to be obtained under the same assumptions. It should also be possible to see the effect of deviating from these results on the resulting diffusivity. Such technique could prove useful in confirming or disproving possible amendments to the original formulation, as well as to inspire new ones if the need arises. Moreover, following this approach should considerably relax the computational requirements. In this section the different ingredients needed for such task are described.

#### 3.5.1 Filtering

The concept of diffusivity of mass is based on a continuous conception of matter. When dealing with a number of individual DEM particles it is necessary to apply some kind of averaging operation to derive the diffusivity field of the system. A natural path to follow is to consider a ball around each point of interest, with a much bigger size than the particles but smaller than the characteristic length scales of the macroscopic problem. By averaging the contribution of each particle falling inside this ball to the variable of interest, an averaged value can be calculated, corresponding to the point on which the ball is centred. Such type of averaging is called spatial averaging, and it is treated in detail in Whitaker (1999). Then, a similar temporal averaging of the individual motions of each particle must be performed to obtain a macroscopic evolution of the spatially-averaged variables. The other way around proceeding is also valid, performing the temporal average before the spatial average, although these operations do not in general commute.

The notion of filtering includes spatial and temporal averages as particular cases. It can be put in rigorous mathematical grounds in a quite general setting. It is the basis of many methods of treating turbulence and numerical methods such as the LES (Sagaut 2002). The basic filtering operation can be expressed as a convolution in a quite general way, as:

$$\bar{u}(t, \mathbf{x}) = \int_{I(t)} \int_{\Omega(\mathbf{x})} u(\tau, \omega) g(t - \tau, \mathbf{x} - \omega) d\omega d\tau \quad (3-58)$$

where  $u$  is the small-scale variable,  $\bar{u}$  is its averaged version,  $g$  is the convolution kernel function and  $I$  and  $\Omega$  represent time and space sets such that  $(t, \mathbf{x}) \in I(t) \times \Omega(\mathbf{x})$ . A natural choice is to take  $I = [t - \Delta t, t]$ ,  $\Omega = B(\mathbf{x}, l)$ , with  $\Delta t$  some short time and  $B(\mathbf{x}, l)$  the ball centred at  $\mathbf{x}$  of radius  $l$ . Furthermore, it is common to take  $g$  of the form:

$$g(t - \tau, \mathbf{x} - \omega) = f(t - \tau) h(\mathbf{x} - \omega) \quad (3-59)$$

where then  $f$  determines the type of time filtering and  $g$  the spatial filtering. The spatial kernel  $h$  is normally taken to be a function that has a single maximum at the point  $\omega = \mathbf{0}$  and tends to zero away from it, becoming very small at a distance comparable with  $l$ . For the time averaging, a one-sided kernel that only depends on the past values is considered, so that it can be calculated as the simulation runs.

In the context of DEM-CFD methods, such strategy can be used to describe the operations needed to perform the backward coupling, in which the effect of the particles is smeared onto the background fluid. The background fluid mesh is used to calculate filtered values, such as the velocity and the solid fraction. The filtering of the solid fraction (the rest of filtered variables are obtained similarly) is now presented begging with its definition:

$$\phi(\mathbf{x}) = I_s(\mathbf{x}) \quad (3-60)$$

where  $I_s$  is the indicator function for the solid, and its value is 1 if the point belongs to a particle and 0 otherwise. The continuum filtered solid fraction (the time averaging is now ignored, since it is just applied in succession and is straight forward) can be written as:

$$\bar{\phi} = \int_{\Omega} h(x - \omega) I_s(\omega) d\Omega \quad (3-61)$$

which can be approximate as:

$$\bar{\phi} \approx \int_{\Omega} h(\mathbf{x} - \omega) \sum_{k|x_k \in B(\mathbf{x}_i, l)} \delta(\mathbf{x}_k - \omega) \frac{V_p(k)}{|B(\mathbf{x}_i, l)|} d\Omega = \sum_{k|x_k \in B(\mathbf{x}_i, l)} h(\mathbf{x}_k - \omega) \frac{V_p(k)}{|B_h(\mathbf{x}_i, l)|} \quad (3-62)$$

where  $\delta$  is Dirac's delta and  $B_h(\mathbf{x}_i, l)$  is the discrete version of the ball, formed by the union of the nodal volumes for all nodes inside the original ball. The nodal volumes are defined, for each node, as 1/4 the sum of all the tetrahedral elements that share that node. Both concepts are illustrated in Figure 3-9. In other words, two approximation errors are being made, both of which tend to vanish as both  $h/l$  and  $a/h$  tend to 0; thus, as long as there are a sufficient number of elements per ball and a sufficient number of particles per element, the error is small.

For each fluid node with index  $i$  a list of neighbouring nodes is considered. This list is defined by those nodes inside  $B(\mathbf{x}_i, l)$ . The weighing function is taken as:

$$h_i(\mathbf{x} - \omega) = \begin{cases} p(\|\mathbf{x}_i - \omega\|) & \text{if } \|\mathbf{x}_i - \omega\| < l \\ 0 & \text{elsewhere} \end{cases} \quad (3-63)$$

where  $p$  is a symmetric, third order polynomial bell centred at the node of interest and which is 0 at the distance  $l$ . In order to determine  $p$ , the ratio height over support is given as an additional input, which in this work is taken as 0.5 in all cases. This parameter, along with the filtering kernel length ( $l$ ) require some tuning to obtain satisfactory results.

### 3.5.2 Derivative Recovery

Once the filtered variables have been determined on the fluid finite element mesh, it is possible to obtain also their derivatives, which might be necessary. For instance, it is shown that the diffusivity can be calculated from the solid fraction gradient, rather than from the solid fraction itself. Since linear tetrahedral elements are being used, the simplest option is to derive the shape functions, yielding piece-wise continuous functions that can be averaged on the nodes. Such method yields an order 1 approximation of the gradients. A more accurate alternative is given by the method of Zhang et al. (2016), which is of second-order accuracy. The method was intended for use in a-posteriori error estimation techniques based on the recovery of the gradient of the solution. It is based on solving a least-squares problem to fit a second-order polynomial to the nodal values, which is then derived to obtain the required derivatives. This method has been chosen to recover the gradient of the solid fraction, which has been adapted from this work DEM-CFD implementation.

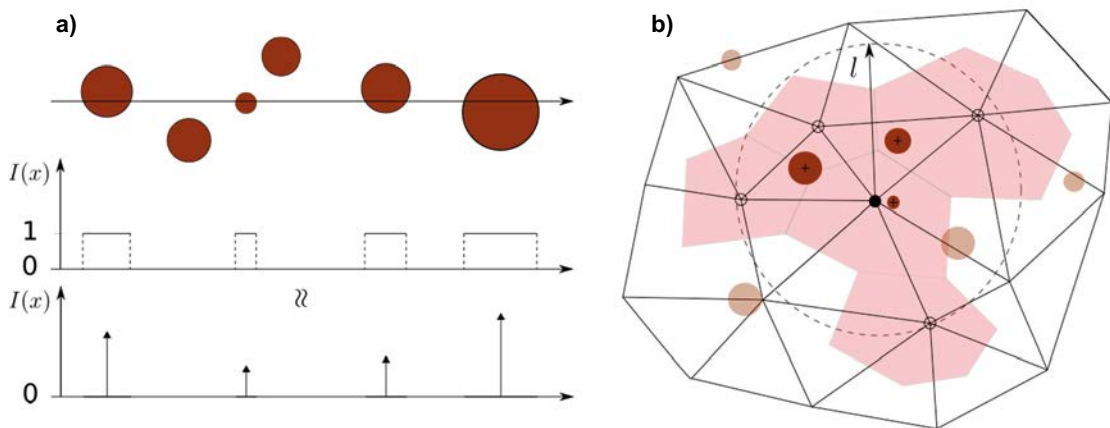


**Figure 3-9.** Approximations in discrete filtering of the solid fraction. The node of interest is marked with a black dot, the neighbouring nodes are marked with a hollow black circle, the nodal areas of these nodes are shaded. The particles that contribute to the calculation of the fluid fraction for the node of interest are depicted in a darker brown colour. Showing: (a) approximation of indicator function by Dirac deltas, the arrows represent the position of the delta's centre and its length represents its coefficient (the particle's volume); and (b) 2D illustration of the approximate representation of the support of the spatial filtering kernel.

### 3.5.3 Calculating the diffusivity

In order to calculate the diffusivity, the following equation is used, it relates it with the solid fraction gradient and the velocity of the continuum description (Liu et al. 2009a):

$$\mathbf{v}\phi = -D\nabla\phi \quad (3-64)$$

where  $D$  is the diffusivity and all forces other than the inter-particle forces and the water resistance have been neglected. This equation suggests a way to calculate  $D$  under different circumstances: take the filtered velocity, interpret it as  $\mathbf{v}$ , do the same with  $\phi$  and recover its gradient (Section 3.5.2). Assuming isotropic conditions, the diffusivity can be represented by a scalar and so it can be calculated by looking at any particular component of  $\mathbf{v}$ , and  $\nabla\phi$ .

This hypothesis holds in the current approach with spheres, although note that Liu et al. (2009a) assumed anisotropic conditions and Equation 3-64 referred to the component orthogonal to the clay interface. It is therefore natural to consider the component orthogonal to the rim.

$$D\phi = -\frac{v_z\phi}{(\nabla\phi)_z} \quad (3-65)$$

where  $z$  is taken as the axis orthogonal to the rim.

This technique has been applied on the free expansion example of Figure 3-10. The results are shown in Figure 3-11, Figure 3-12 and Figure 3-13, where the values have been normalised by the predicted value by the theory presented in Liu et al. (2009a). The results show the expected order-of-magnitude agreement everywhere, except near the middle, where the values reach spikes of an order of magnitude over the expected values. These spikes are shown as dark spots because the values do not fall within the ranges shown in the legend. It was not possible to remove them even by changing the support radius of the filter ( $l = 1.5 \times 10^{-6}$  was used). However, note that near the middle, the filtered particles velocity changes sign and so does the solid fraction, so that Equation 3-64 must fail at some point there. On the other hand, note that the individual particles do move around the middle and this introduces a noise that might overpower the mean signal when it becomes very small. This matter should be studied further.

In any case, this is the kind of result that could be used to improve the understanding of the behaviour of the sol and to modify the macroscopic equations if the right system is chosen. Even if the use of spherical particles leads to just confirm the diffusivity function of the macroscopic formulation, the possibility to then add other effects exists, effects such as the shape of the particles and study it from the microscopic perspective. This could then be used to 'correct' the original equations and consider this effect. This is further discussed in Section 3.6.

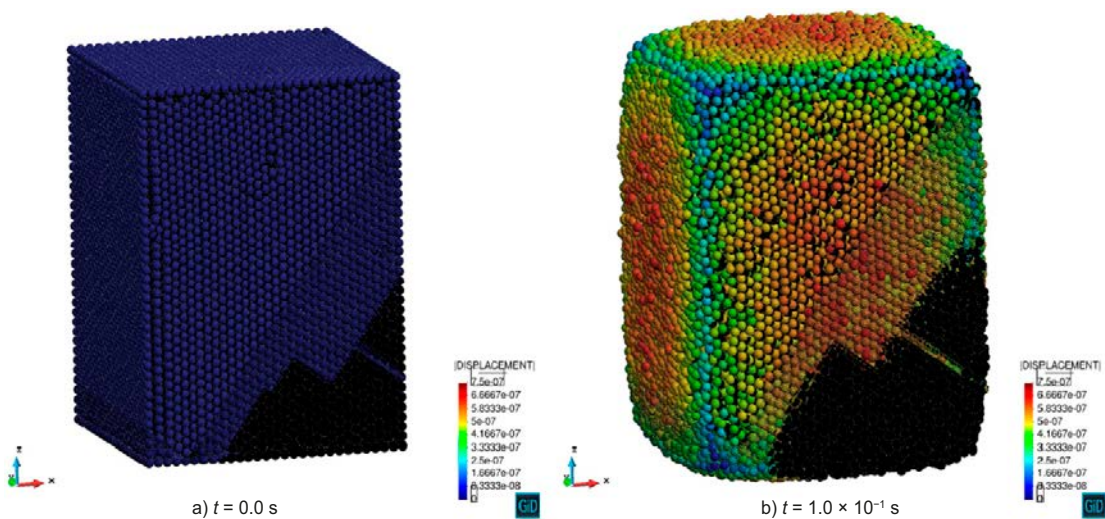


**Figure 3-10.** Example of free expansion of a block of clay. Initial average separation corresponds approximately to a solid fraction of 0:01, with a cation concentration of  $c = 1 \times 10^{-4}$  mmol.

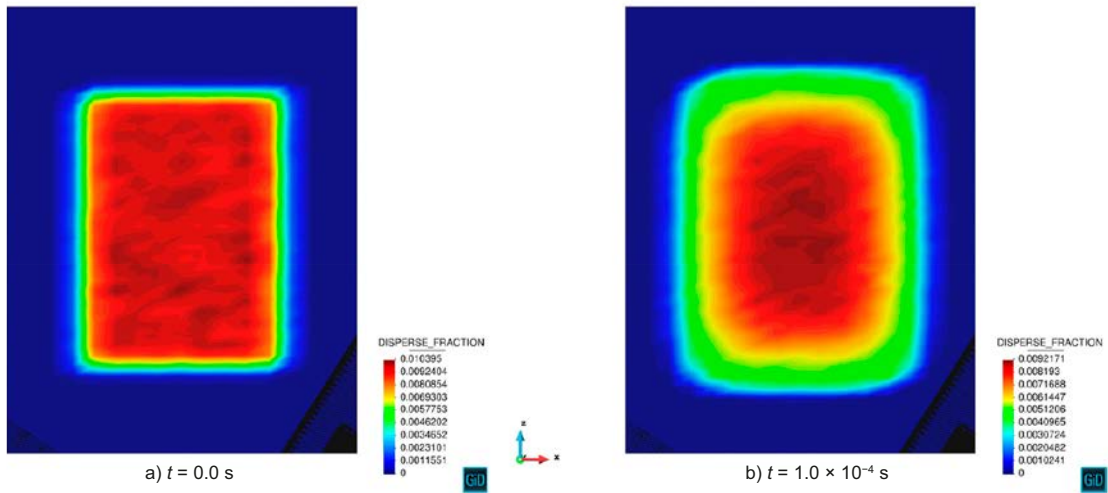


**Figure 3-11.** Mid-section cut of the background mesh from the same simulation as Figure 3-10. The contour plot shows the altered solid fraction on the background mesh.

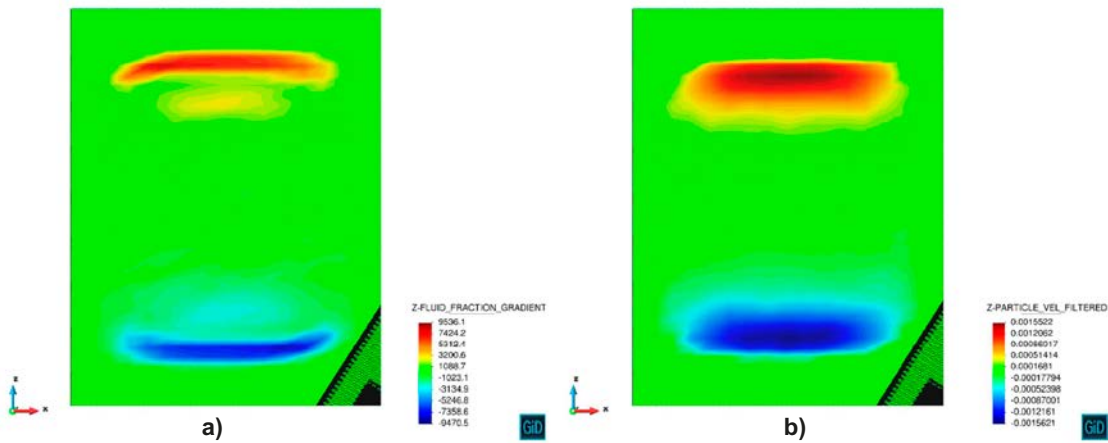


**Figure 3-12.** Mid-section cut of the background mesh from the same simulation as Figure 3-10. The contour plot shows the filtered z-components of the fluid fraction gradient (a) and the particles' velocity (b) on the background mesh.

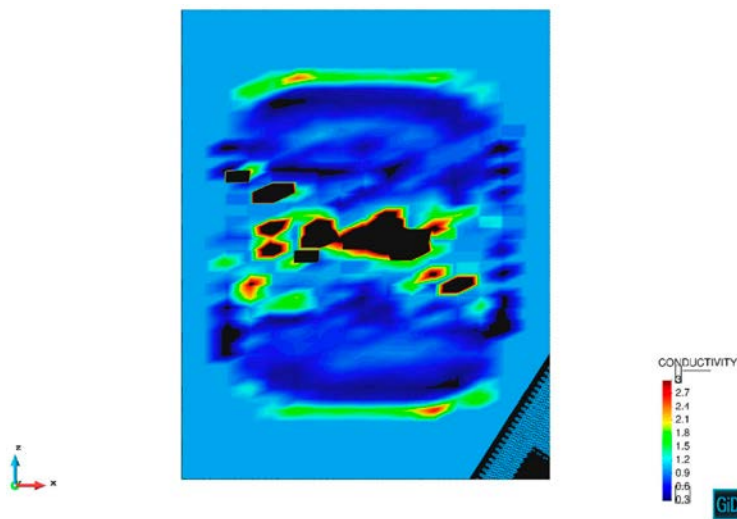


**Figure 3-13.** Diffusivity obtained from Equation 3-65,  $t=1 \times 10^{-4}$  s.

## 3.6 Future developments

### 3.6.1 The need for further developments

The current developments reported in this document are not sufficient to resolve the accuracy problems of the model proposed by Neretnieks et al. (2017). Nonetheless, it has been shown that it is possible to model the expected macroscopic behaviour (the correct rate of diffusivity) by implementing Liu's et al. (2009a, b) theory in a particle-based code, at least for the simple case of free expansion.

Furthermore, the introduction of individual particles brings about new possibilities because of the richer range of scales that are now accessible. Indeed, the current most promising theory to explain the observed inconsistencies between theory and experiments is based on phenomena that occur at a smaller scale, smaller than that accessible to the macroscopic description: flocculation. Unfortunately, the current implementation is still not capable of reproducing this type of behaviour, which is fundamentally linked to particles anisotropy.

In this section, the most important areas where the need for further developments has been identified are discussed. Improvement are focused on capturing with enough fidelity the fundamental physics that govern the development of the rim-zone and the rate of clay erosion by the incoming flow.

### 3.6.2 Realistic particle shapes and the study of flocculation

As mentioned above, the macroscopic method used by Neretnieks et al. (2017) cannot explain the increased rates of erosion observed in the experiments presented in Schatz et al. (2013). The observation of agglomerate formation led these authors to propose a modification of their method by introducing the empirical parameter  $\phi_{R,f}$ , defining the solid fraction at which flocculation occurs. This parameter, together with assumptions about the behaviour of the system after the formation of flocs allowed the authors to fit the erosion rate results with reasonable accuracy. However, this solution is unsatisfactory because it relies on a theory that is completely untested (i.e. the process of floc formation at a microscopic scale and its impact on the transport of clay). This conclusion was already reached by them, recognizing the need for further studies.

The process of flocculation is based on the edge-face attraction forces that are known to develop in smectites (Neretnieks et al. 2017). At low volume fractions, the particles are mainly stacked in 'deck-off-cards' formations and cannot rotate freely to form the loose 'house-of-cards' formations that make up the flocs.

An interesting topic of further research would be to consider DEM particles with more realistic shapes. One option is to use coin-like particles. This technology implies some additional computational costs compared to spheres, but those are not expected to go beyond one order of magnitude per particle and time step. One order of magnitude is not such a large difference in 3D simulations, as doubling the size of the domain already implies increasing eight times the number of particles. These additional costs would mainly come from the increased difficulty in computing the overlaps, that would now involve more complicated computations (edge-edge contact and edge-face contact considering varying orientations). Another possibility is to consider polyhedral particles. Such polyhedron could be formed by the same rigid face elements that are already in use in our code. Again, increased costs are expected.

Another aspect linked to the shape is the anisotropy of the force potentials that have been assumed to be isotropic. With the implementation of more realistically-shaped particles, allowing the introduction of anisotropic force potentials could be easy, as they would be based on the same coordinate management used to track the contacts.

### 3.6.3 Hydrodynamic interactions

It has already been argued in Section 3.3.2 that the hypothesis of single-particle theory built into Liu's et al. (2009a, b) theory is a strong hypothesis. To study the evolution of a collection of particles, the inclusion of rotation and flocculation effects might not be enough.

More broadly, many-body nature of hydrodynamic interactions can be studied with methods such as Stokesian Dynamics (Durlinsky and Brady 1989). However, these methods are computationally very expensive, precisely due to the many-body coupling, which induces the need to invert very large, full matrices. Some authors have taken an intermediate step that looks promising for the present context, they consider only the dominant terms in the long-range expansion of the hydrodynamic interaction formula. These terms can be expressed as pair/wise interactions, resembling the contact models of DEM. For instance, Varga et al. (2015) studies the dynamics of colloidal gelation with such approach.

### 3.6.4 Coarse Graining

In Section 3.2.1, the extent of the rim zone, where the phenomena of interest mainly take place, was calculated to reach:  $\delta_{rim}(x) \sim 0.01\sqrt{x}m$ . The computational cost estimations seem to point to an excessive cost, even when taking into consideration a small portion of this thin rim region.

Nonetheless, the possibility of decreasing the simulated number of particles to simulate the same domain must be considered with the goal of lowering the computational requirements. Such coarse graining procedure must be done ensuring the preservation of relevant physical properties. In this context, the main interest is put in the clay diffusivity. When using fewer, larger virtual particles the same upscaled diffusivity should be recovered.

Considering Equation 3-4, the original volume fraction is maintained but the forces are changed to obtain the same resulting diffusivity. The idea is to apply a transformation that violates the geometric similarity, but only in relation to the length scales of the particles relative to the length scales of the domain, while keeping the similarity within the particles systems. The resulting system should behave approximately in the same way, as long as these scales are still properly separated (Padding and Louis 2006).

For the sake of simplicity, the effect of thermal diffusion (which is significantly smaller than that produced by the van der Waals and DDL forces) is disregarded. Thus, the modified forces  $F_{vdw}^0$  and  $F_{DDL}^0$  are considered, also the scaling parameter  $\alpha$  such that all the dimensions are multiplied by it after the transformation.

$$D'(ah, \alpha a) = D(h, a) \quad (3-66)$$

where  $D'$  is defined as in Equation 3-4 by replacing the forces by their modified counterparts, the dependence on  $h$  and  $a$  is introduced to highlight the parameters that have been modified by the transformation. Both forces are defined as:

$$F'_{vdw}(h) = \frac{1}{\alpha} F_{vdw}(h) \quad (3-67)$$

$$F'_{DDL}(h) = \frac{1}{\alpha^3} F_{DDL}\left(\frac{h}{\alpha}\right) \quad (3-68)$$

with these definitions the resulting diffusion should be the same as in the original system.

This approach has not been explored in the simulations, although, it would only be of real utility in the direct approach, where the relative size of the particles with respect to the boundaries of the domain could be increased. Other scaling schemes are possible and have been systematically applied in Padding and Louis (2006) in a process that the authors called “telescoping down”. There, the ranges of scales of the problem are significantly narrowed, while still preserving the same hierarchy and a good separation between them. The technique is promising for the present problem, as this great separation of scales has proved to be one of the greatest hurdles.

Another possibility to explore, in relation to the above telescoping down of scales, is to modify the inter-particle potentials of the problem (lowering their stiffness), what forces the use of extremely small time-steps. This would be analogous to what is routinely done in regular DEM simulations, where the stiffness of the contact models can be lowered by several orders of magnitude without significantly altering the behaviour of the system.

### 3.6.5 Boundary conditions

Even though a considerable amount of work has been dedicated to advance in this direction, there are still important questions to be answered in this subject. The matter of how to design appropriate boundary conditions for the direct approach deserves further exploration. The goal is to be able to set a domain that is small enough to be simulated while it is still representative of the system and can yield the desired output, such as the erosion rate.

### 3.6.6 The possibility of implicit time stepping

The standard approach of DEM methodology uses explicit time integration. The reason for this lies in the frequent neighbour changes that take place in regular applications of the method, which tend to make implicit methods less competitive. In the present context, the suspended particles spend increasingly long times with the same neighbours. Thus, it seems possible that an implicit approach to the problem might prove more efficient. After all, given the exponential damping of the expansion process unaffordable simulated times are yielded. An interesting point to consider in future research is if this is the best way to simulate the clay particles.

## 3.7 Concluding Remarks & Outlook

Section 3 explores the DEM as a way to study the development and erosion of the clay sol that forms at the rim region. The characteristic scales of the problem have been studied to assess the viability of this kind of approach. Some difficulties in applying the direct approach have been found, particularly with the direct use of particles to calculate the erosion rate of clay at the rim region under the influence of an incoming flow. The main issue with this kind of approach is the extremely long times needed to reach the steady state, or at least a sufficiently developed solution.

Nonetheless, a set of numerical tools to adapt an existing CFD-DEM application to this problem have been developed, including: (1) a new particle object to deal with the particular potentials and specific fluid-coupling characteristic of the clay particles; (2) a new integration scheme based on the velocities, given that the relaxation time of the particles is extremely low due to their tiny mass; (3) a periodic version of the search algorithm and force calculation to be able to run periodic domains filled with sol; (4) a new type of inlet, the force inlet, which imposes an injection force to simulate the gel-sol interphase with a fixed solid fraction boundary condition; (5) a tool to calculate fluxes through surfaces; (6) a new set of filtering tools; and (7) and a new type of imposed fluid velocity based on the local viscosity.

Furthermore, an intermediate approach has been proposed as an alternative, consisting in studying upscaled properties for the macroscopic description of the system. Specifically, it has been shown how the diffusivity may be recovered from the system being an appropriate way to approach the problems. The diffusivities are consistent with the model presented in Liu et al. (2009a, b), except for a region with some noise (this has been attributed to the extremely low values of the solid fraction gradient).

It has been acknowledged that the current technology is not enough to answer the difficult questions posed in Neretnieks et al. (2017) and that more developments are needed. The most important tasks could be: (1) the development of flat coin-like or polyhedral particles to better model the real shape of the clay ones; (2) the study of the importance of hydrodynamic interactions, which are only treated in an upscaled way by the present model, being based on a static porous medium conception of the medium that might not be; (3) the exploration of several techniques to narrow down the range of scales present in the problem, including the telescoping down of scales (Padding and Louis 2006) and the stiffness softening of the potentials; and (4) the consideration of implicit strategies that might speed up the simulations, especially when the process slows down as the rim region relaxes toward steady-state.

## 4 Simulation of experimental tests with a soil mechanics model

The objective of this section is the characterisation of bentonite swelling experiments with a finite element implementation of the expansive soil mechanics model reviewed (Alonso et al. 1999). Two free swelling tests are firstly simulated to serve as model calibration. Once the implementation is calibrated, its applicability to swelling in a fracture experiments is discussed based on a number of additional simulations.

### 4.1 Modelling approach

A set of simulations has been run in Code\_Bright (Olivella et al. 1996), a 3D finite element software developed at the Department of Geotechnical Engineering and Geo-Sciences of the Technical University of Catalonia (UPC). This code has been especially designed to perform coupled thermo-hydro-mechanical (THM) analysis in porous media and is able to solve multiphase flow coupled to non-linear soil mechanics models.

The Barcelona Expansive Model (BExM, Alonso et al. 1999), an elastoplastic constitutive law for expansive clays, has been chosen as the constitutive law for bentonite. This elastoplastic advanced soil mechanics model was developed for expansive clays. The most representative characteristic is the definition of two different structural levels: macrostructure and microstructure. This bentonite characterisation method accounts for: aggregate deformation (micro-swelling), macrostructural porosity competition and the relation between microstructural elastic strains and plastic macrostructural deformation. No chemical effects are included in this model and have therefore not been considered in this first stage of the project.

Mechanical parameters are extracted from previous work by Navarro et al. (2014, 2016) and through calibration with free swelling experiments. The included parameters for elasticity, plasticity, and hydro-mechanical couplings are presented in Table 4-1. The HM coupling process is done by relating pressure and void ratio. These relations are specified through the following formulation:

$$f^{SD} = f_{sd0} + f_{sd1} \left( 1 - \frac{p}{p_0} \right)^{n_{sd}} \quad (4-1)$$

$$f^{SI} = f_{si0} + f_{si1} \left( \frac{p}{p_0} \right)^{n_{si}} \quad (4-2)$$

where  $f^{SD}$  accounts for microstructural swelling and  $f^{SI}$  for microstructural compression, both considering the ratio between net mean stress and net mean yield stress at the current suction level ( $p/p_0$ ), as shown in Figure 4-1. For the modelling of macrostructural water flow, a conventional Darcian formulation is used:

$$q_M = - \frac{k_M \cdot \kappa_M}{\mu_W} \cdot (\nabla P_L + \rho_W \cdot g \cdot \nabla z) \quad (4-3)$$

where  $k_M$  ( $m^2$ ) is the isotropic intrinsic permeability of the macrostructural liquid ( $7.8 \times 10^{-21} m^2$ ),  $\mu_W$  ( $Pa \cdot s$ ) dynamic viscosity of water,  $P_L$  ( $Pa$ ) macrostructural liquid pressure,  $\rho_W$  ( $kg/m^3$ ) water density,  $g$  ( $m/s^2$ ) gravity constant,  $z$  ( $m$ ) the vertical coordinate and  $\nabla$  the gradient differential operator.  $\kappa_M$  (-) is the macrostructural relative permeability, modelled using the Brooks and Corey (1964) and Burdine (1953) formulation:

$$\kappa_M = S_M^{\frac{(2+3\lambda)}{\lambda}} \quad (4-4)$$

where  $S_M$  is the macrostructural degree of saturation and  $\lambda$  the pore size distribution index (a value of 3 has been used).

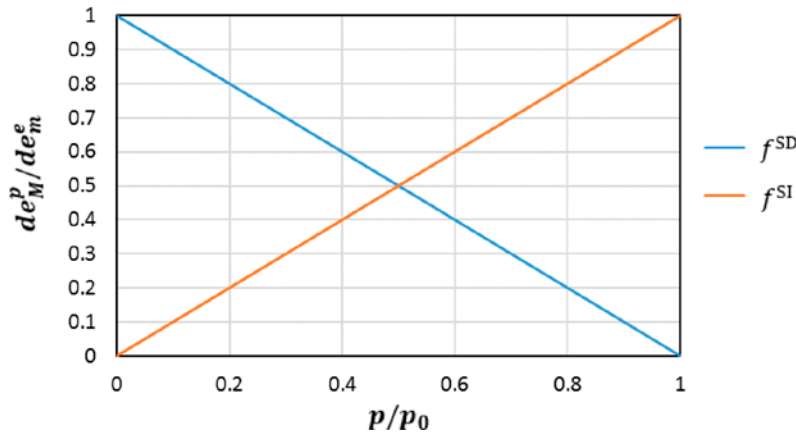


**Figure 4-1.** Graphical representation of “*f*” functions in terms of the ratio  $p/p_0$  in the isotropic stress state, where  $p$  is the net mean stress and  $p_0$  is the net mean yield stress at the current suction.  $f^{SD}$  when microstructural swelling is produced ( $e_m$  increases) and  $f^{SI}$  for microstructural compression ( $e_m$  decreases).

A classical van Genuchten (1980) retention curve model was used to relate suction and saturation degree:

$$\frac{S_M - S_{M,0}}{1 - S_{M,0}} = [1 + (\alpha \cdot s)^n]^{-m} \quad (4-5)$$

where  $S_{M,0}$  is the macropore residual degree of saturation and  $s$  represents suction. The curve is fitted with the parameters  $\alpha = 3.74 \times 10^{-5} \text{ kPa}^{-1}$ ,  $m = 0.45$  and  $n$  assumed equal to  $1/(1 - m)$ . These are identified from the experimental water content data obtained by Pintado et al. (2013).

For the bentonite clay, the solid phase particle density is fixed to  $\rho_s = 2.78 \text{ g/cm}^3$  and the liquid density to  $\rho_l = 1 \text{ g/cm}^3$ .

**Table 4-1. Mechanical and coupling parameters for bentonite buffer material using BExM by Alonso et al. (1999).**

Elastic parameters							
$\kappa_{\text{Macro}}$	$\kappa_s$	$\nu$	$K_{\text{min}}^{\text{Macro}}$ (MPa)	$\kappa_{\text{micro}}$	$K_{\text{min}}^{\text{micro}}$ (MPa)		
0.05	0.25	0.35	1	0.08–0.3	1		
Plastic parameters							
$M$	$r$	$\beta$ (MPa <sup>-1</sup> )	$k_s$	$P_c$ (MPa)	$p_o^*$ (MPa)	$p_{t0}$ (MPa)	$\lambda(0)$
1.07	0.8	0.02	0.1	0.01	10.4	0	0.15
Coupling parameters							
$f_{sd0}$	$f_{sd1}$	$n_{sd}$	$f_{si0}$	$f_{si1}$	$n_{si}$		
0	1	1	0	1	1		

## 4.2 Free swelling test I

The first modelled experiment accounting for bentonite expansion is the one presented by Sane et al. (2013). This test consists of a bentonite sample under free vertical swelling in a water saturated tube. Although the experiments were carried out with different wetting solution salinities, the modelled one refers to the test carried out with de-ionised water.

### 4.2.1 Model setup

The clay sample has a cylindrical shape with 40 mm height and a diameter of 50 mm. The model considers a 2D axisymmetric setup assuming a rectangular section of 40 × 25 mm (Figure 4-2). Spatial discretisation has been performed using 60 rectangular elements. The temporal extension of the simulation has reached 200 hours.

Initial bentonite conditions include: a dry density of  $1.73 \text{ g/cm}^3$ , 17 % of gravimetric water content, a total void ratio of 0.6 (porosity of 0.375) with values for macroporosity and microporosity of  $\sim 0.191$  and  $\sim 0.187$ , respectively. Initial relative liquid pressure is established to  $-22.62 \text{ MPa}$ .

Axisymmetric conditions are considered on the left side of the domain, applying to both mechanical and flow processes. Other mechanical conditions are fixed null normal displacement in the bottom and right boundaries and free movements in the top side. For flux, no flow is allowed to exit the bottom and right boundaries and a water saturated condition is applied on the top boundary.

#### 4.2.2 Results

The results of the simulation of the first free swelling test performed in this work are compared to experimental values from Sane et al. (2013) in Figure 4-3 in terms of vertical swelling displacements. The results compare relatively well with experimental data (Figure 4-3). It may be concluded that the expansion process characterisation is correctly captured with this model. Figure 4-4 presents temporal evolution of porosity and micro void ratio in the uppermost point of the sample and spatial porosity distribution after 200 hours of experiment. The results indicate a maximum porosity of 0.64 after 200 hours, corresponding to a dry density of  $\sim 1 \text{ g/cm}^3$ .

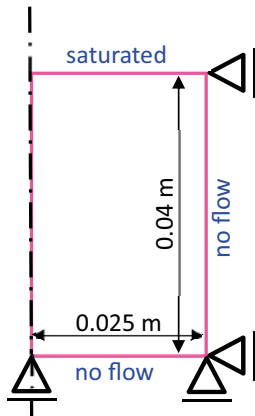


Figure 4-2. Geometrical description and boundary conditions of free swelling test I.

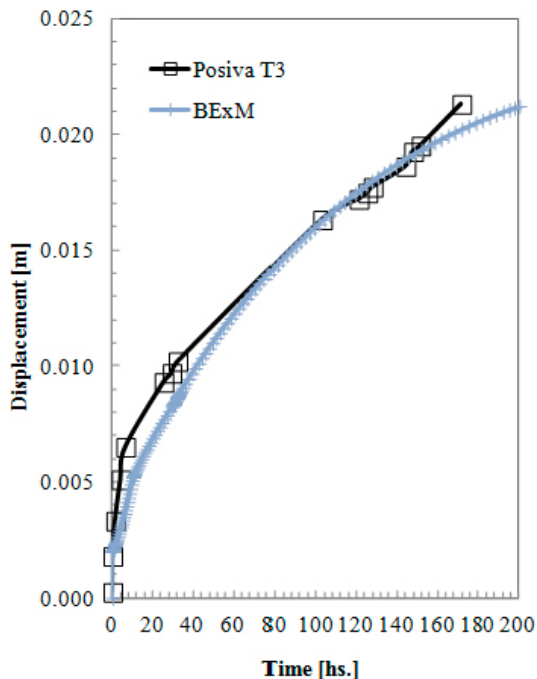
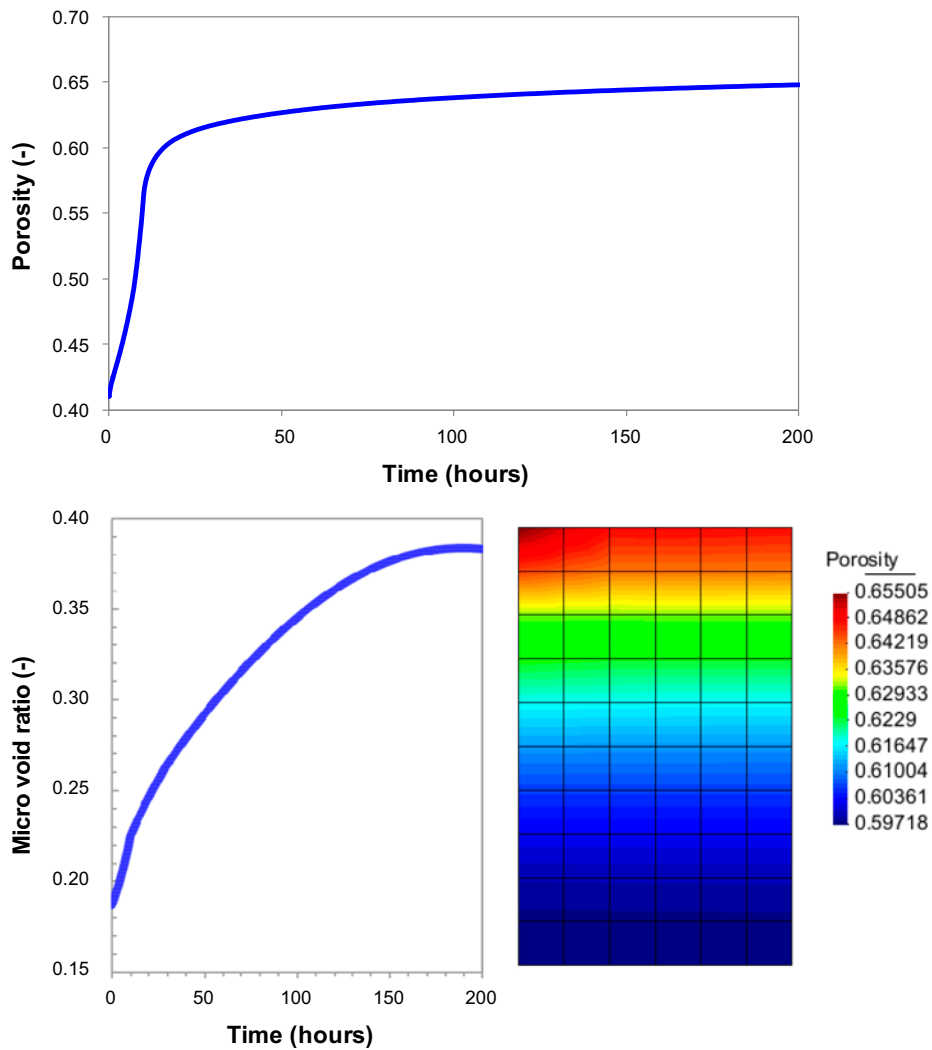


Figure 4-3. Bentonite swelling displacements (m) evolution with time: comparison between modelled (this work) and experimental results (Sane et al. 2013).



*Figure 4-4. Temporal evolution of porosity (top) and micro void ratio (bottom-left) for the uppermost point of the sample and spatial porosity distribution after 200 hours (bottom-right).*

### 4.3 Free swelling test II

A second bentonite free vertical expansion test has been simulated in order to verify the calibration accomplished in the first model. This second test will also serve as connection with the erosion in a fracture experiment, since initial material conditions are quite similar. The modelled laboratory test is very similar to the previous one (Section 4.2). The main differences are the use of a different geometry and material. The results of the experimental test by Sane et al. (2013) are extracted from Navarro et al. (2014).

#### 4.3.1 Model setup

Similar to Section 4.2, the simulation considers a 2D axisymmetric setup with rectangular geometry. In this case the dimensions are  $15.85 \times 25$  mm. The finite element mesh has  $6 \times 5$  rectangular elements. The simulated time is 55 hours.

Slightly different initial conditions for the bentonite material are considered:  $1.6 \text{ g/cm}^3$  for dry density, a 17 % of water content, a total void ratio of 0.74 and a total porosity of 0.424. Boundary conditions for flow and mechanical behaviour are set in the same way than in the first experiment (see Section 4.2).

### 4.3.2 Results

As in the previous experiment, Figure 4-5 and Figure 4-6 present model results and the comparison with some experimental measurements. Reasonable matching in swelling distances confirms a good model calibration. In terms of porosity and micro void ratio, results are qualitatively similar to those of the first swelling test. Differences in geometry and initial material conditions lead to a faster swelling process in terms of time lapse.

## 4.4 Erosion in a fracture test

The model calibrated using the free swelling tests (Sections 4.2 and 4.3) is used here to simulate an experiment where bentonite clay is saturated and expands into an artificial fracture intersecting the sample. The experiment setup and results are extracted from the work by Schatz et al. (2013). The goal is to study the applicability and limitations of such soil mechanics-based models to simulate the problem of bentonite extrusion into a fracture.

Dense bentonite sample cylindrical tablets with a height of 20 mm and a diameter of 20 mm were prepared with an actual montmorillonite dry density of  $1.59 \text{ g/cm}^3$ . Assuming a montmorillonite content in the range of 75 to 90 %, the effective montmorillonite dry density (EMDD) of the bentonite sample is in the range  $1.275$  to  $1.434 \text{ g/cm}^3$ . The initial porosity is 0.42, assuming a bentonite grain density of  $2.78 \text{ g/cm}^3$ .

The experimental setup is shown in Figure 4-7. The cell used in the experiments is made of acrylic blocks and has dimensions of  $240 \times 240 \times 40 \text{ mm}^3$ . It contains a hosting cylindrical chamber in the centre (2 cm high), where the clay sample is confined. The cell considers a horizontal artificial fracture with an aperture of 1 mm across the entire cell mid-section. Different flow holes are included in the cell: on both sides of the hosting chamber (to provide additional saturation interfaces), in the inflow side of the cell (connected to a peristaltic pump to provide flow condition), and in the outflow end (output channels to enable eroded effluent collection for analysis). More details can be found in Schatz et al. (2013).

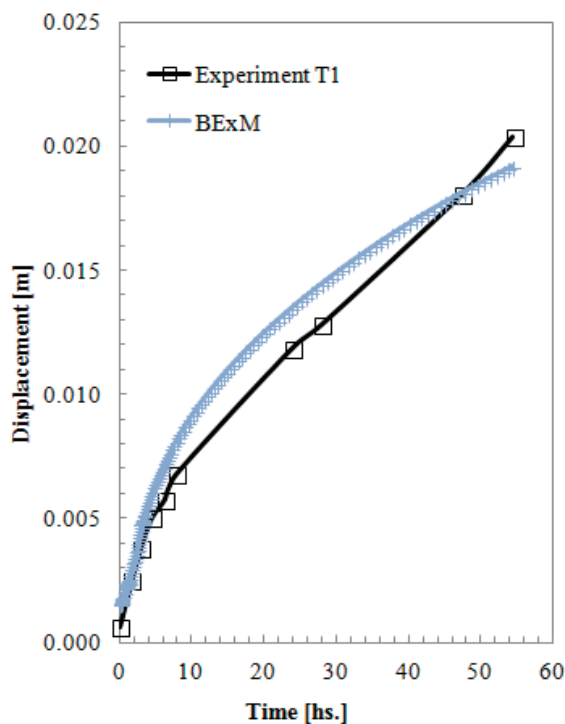


**Figure 4-5.** Bentonite swelling distance evolution with time, comparison between modelled and experimental results (Sane et al. 2013).

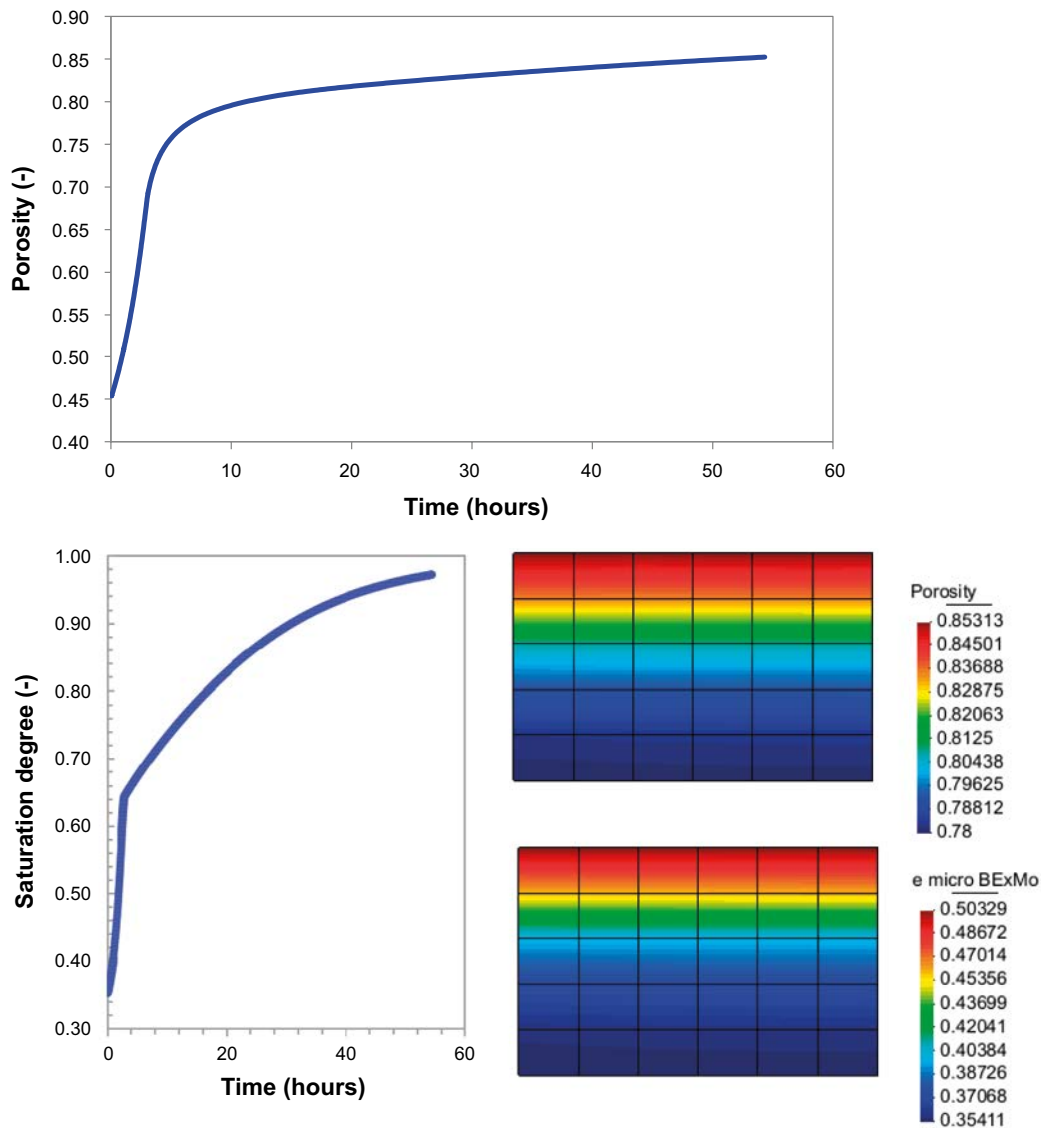


**Figure 4-6.** Temporal evolution of porosity (top) and saturation degree (bottom-left) for the uppermost point of the sample; spatial distribution of porosity and micro void ratio after 200 hours (bottom-right).

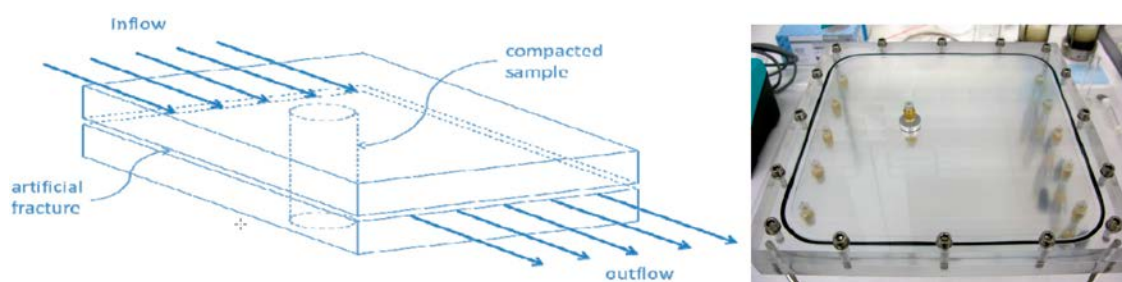


**Figure 4-7.** Schematic representation and photographic image of the flow-through, artificial fracture test system (from Schatz et al. 2013).

Different experiments were carried out over a range of conditions including different bentonite and water solution compositions, and different flow rates along the fracture. The test modelled in this study corresponds to test 11 of Schatz et al. (2013) and considers sodium montmorillonite, de-ionised water and a zero-flow rate. The total duration of the experiment reached 720 h. Different simulations have been carried out to characterise this experiment, as detailed below.

#### 4.4.1 Model setup

Given that the test considers the extrusion of a cylindrical sample into a fracture where no external flow rate is imposed, the model setup can realistically consider 2D axisymmetric conditions. The symmetry axis coincides with the axis of the cylindrical chamber in Figure 4-7. In addition, a horizontal symmetry plane at mid-height of the fracture thickness is also considered to reduce the size of the model. The 2D axisymmetric model is solved in Code\_Bright (Olivella et al. 1996). The 2D geometry is depicted in Figure 4-8 and includes a squared bentonite sample region of  $10 \times 10 \text{ mm}^2$  on the left side and half of the fracture thickness in the lower right part ( $0.5 \times 24 \text{ mm}$ ). Above the fracture, a linear elastic acrylic domain is included ( $9.5 \times 24 \text{ mm}$ ) to explicitly consider the stiffness of the cell. Even though the total duration of the experiment was 720 h, convergence issues in the constitutive law prevented the model to reach this time, as detailed below.

The initial conditions for sodium montmorillonite consider a dry density of  $1.59 \text{ g/cm}^3$ , a water saturation of 26.5 %, and a total porosity of 0.42 (void ratio=0.74). The acrylic domain is modelled as a stiff linear elastic domain with a Young's modulus of 3 GPa and a Poisson ratio of 0.35. Bentonite properties are equivalent to those used in the free swelling simulations, presented in Table 4-1. The calibrated parameters extracted from these free swelling simulations were used.

Several models differing in geometry and boundary conditions have been implemented using these material properties in an attempt to explain the experimental results. The geometry and boundary conditions of each of these models are presented below. All of them consider a 2D axisymmetric setup.

In addition, a set of sensitivity cases was carried out to assess the impact of flow boundary conditions on the results in terms of expansion. Namely, in this sensitivity study the clay material is saturated only through the fracture (the top boundary is considered closed to flow). Due to the very small differences in the obtained results, these results are not presented.

#### Fracture model

A simpler model has been set up to avoid geometrical disturbances in the region of the acrylic corner caused by the continuity in the displacement field between bentonite and acrylic. Its geometry is shown in Figure 4-9 and only includes the first vertical half millimetre of the bentonite sample. The 2D model only represents the clay domain with a section of  $0.5 \times 1.0 \text{ mm}$ , representing a 1D extrusion problem. Besides the two symmetry constraints in left and lower boundaries, vertical displacements are prevented at the top boundary, while bentonite is free to deform on the right side (i.e. at the swelling/extrusion boundary). Finally, saturated conditions are imposed at the upper and right boundaries.

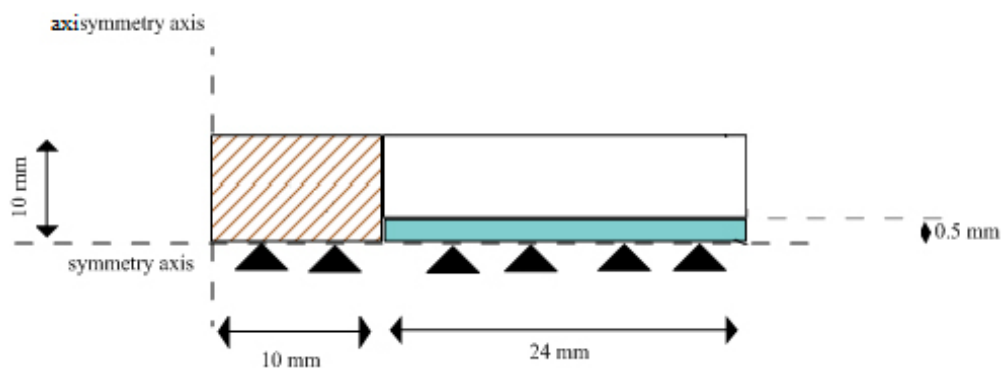


Figure 4-8. Geometrical description of the 2D section of the simulated extrusion in a fracture test.

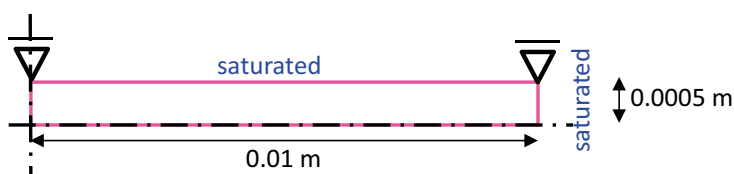


Figure 4-9. Geometry, dimensions and boundary conditions for the bentonite-fracture mode.

Element size decreases gradually when approaching the right boundary, where higher de-structuring is expected. The total simulation time is restricted to 10 hours due to numerical convergence issues in the constitutive model when reaching large deformations.

**Clay block model**

This model considers the entire clay sample as a square with dimensions  $10 \times 10$  mm, as shown in Figure 4-10. The difference with the first trial model is that in this case the fracture and acrylic domains are considered as boundary conditions. The boundary conditions included symmetry constraints in left and lower boundaries. Normal displacements are restricted and saturated conditions are imposed at the top boundary of the bentonite sample. On the right boundary, bentonite is free to deform at the interface with the fracture (first 0.5 mm), while saturated conditions are imposed. Normal displacements are restricted in the upper part of the right boundary to simulate the acrylic constrain. Spatial discretisation is refined in vertical and horizontal directions towards the bottom right corner. The total simulation time is restricted to 5 hours in this case due to numerical convergence issues in the constitutive model when reaching large deformations.

**Complete cell model**

The last model is similar to the first trial, with the exception of the treatment of the bottom-right corner of the bentonite sample. The dimensions of the model are  $10 \times 34$  mm (Figure 4-11). In this model, special attention is given to the acrylic left-bottom corner. The corner region (with a dimension of  $1.0 \times 1.0$  mm) is implemented with a less stiff Young’s modulus (0.4 GPa) compared to the remaining acrylic domain, in an attempt to reduce the effect of displacement continuity between acrylic and bentonite on the modelled expansion. The same finite element mesh as in the clay block model is used for the bentonite domain. The total simulation time is restricted to 10 hours in this case due to numerical convergence issues in the constitutive model when reaching large deformations.

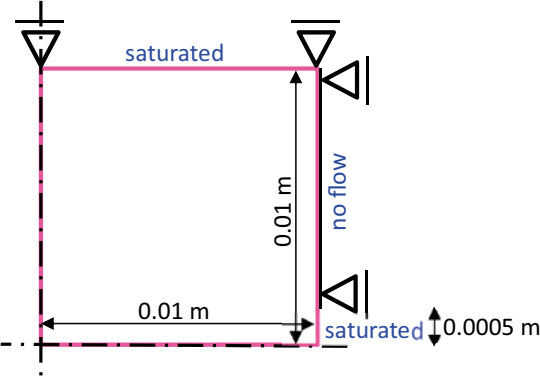


Figure 4-10. Geometry, dimensions and boundary conditions for the clay block model.

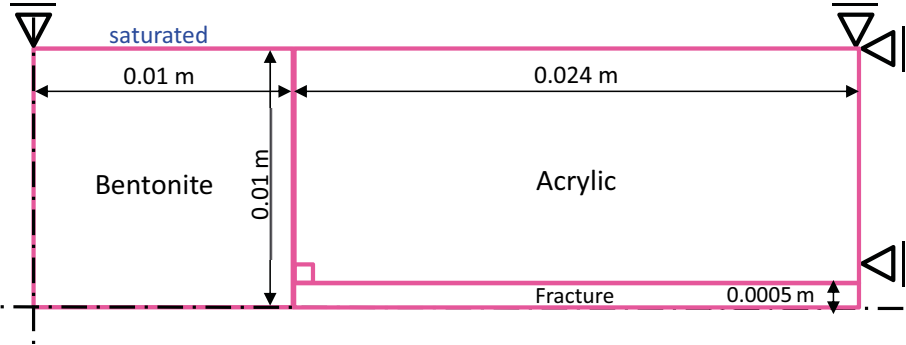
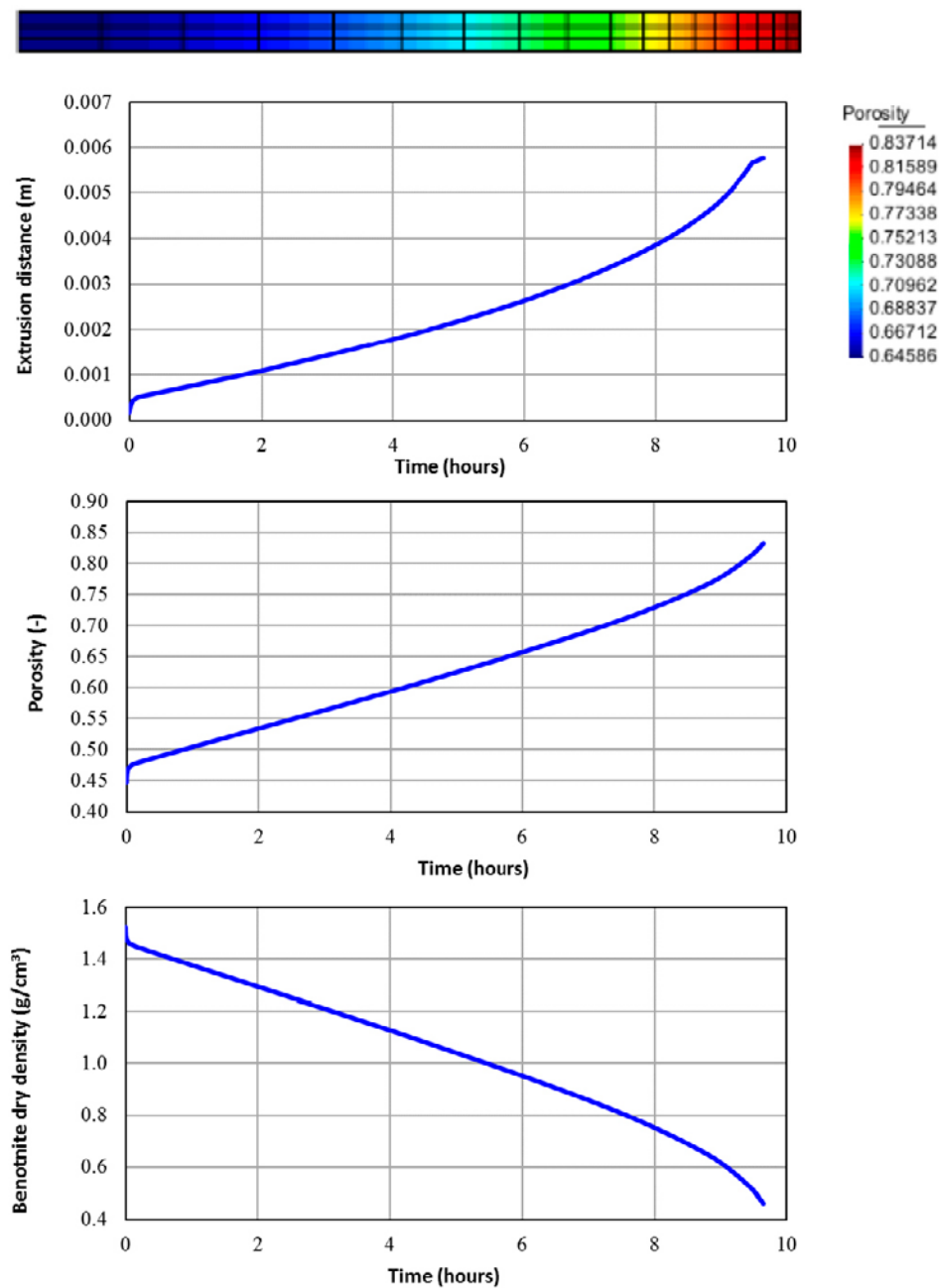


Figure 4-11. Geometry, dimensions and boundary conditions for the complete cell model: bentonite, fracture, acrylic, and a less stiff wedge.

#### 4.4.2 Results

The results of the 2D axisymmetric models presented in Section 4.4.1 are discussed in this section. 2D spatial distribution plots correspond to the final simulated time in each model. In addition, the evolution in time of the displacement of the point in the bentonite sample in contact with the fracture is shown in 1D plots.

The results of the fracture model, clay block model, and complete cell model are presented in Figure 4-12, Figure 4-13, and Figure 4-14, respectively, in terms of porosity, displacements, and dry density evolution. Finally, to compare the model and experimental results, Figure 4-15 shows the dry density of the material present in the fracture after each simulation and its comparison with experimental data from Schatz et al. (2013). The model results in Figure 4-15 consider the mass of bentonite that falls at the right of the initial position of the bentonite-fracture interface. However, it should be noted that the experimental results correspond to the final state of the experiment after 720 hours, while model results were only obtained for 10 hours at the most due to numerical convergence issues.



**Figure 4-12.** Porosity (-), horizontal displacement (m) and dry density (g/cm<sup>3</sup>) results for the fracture model after 10 h.

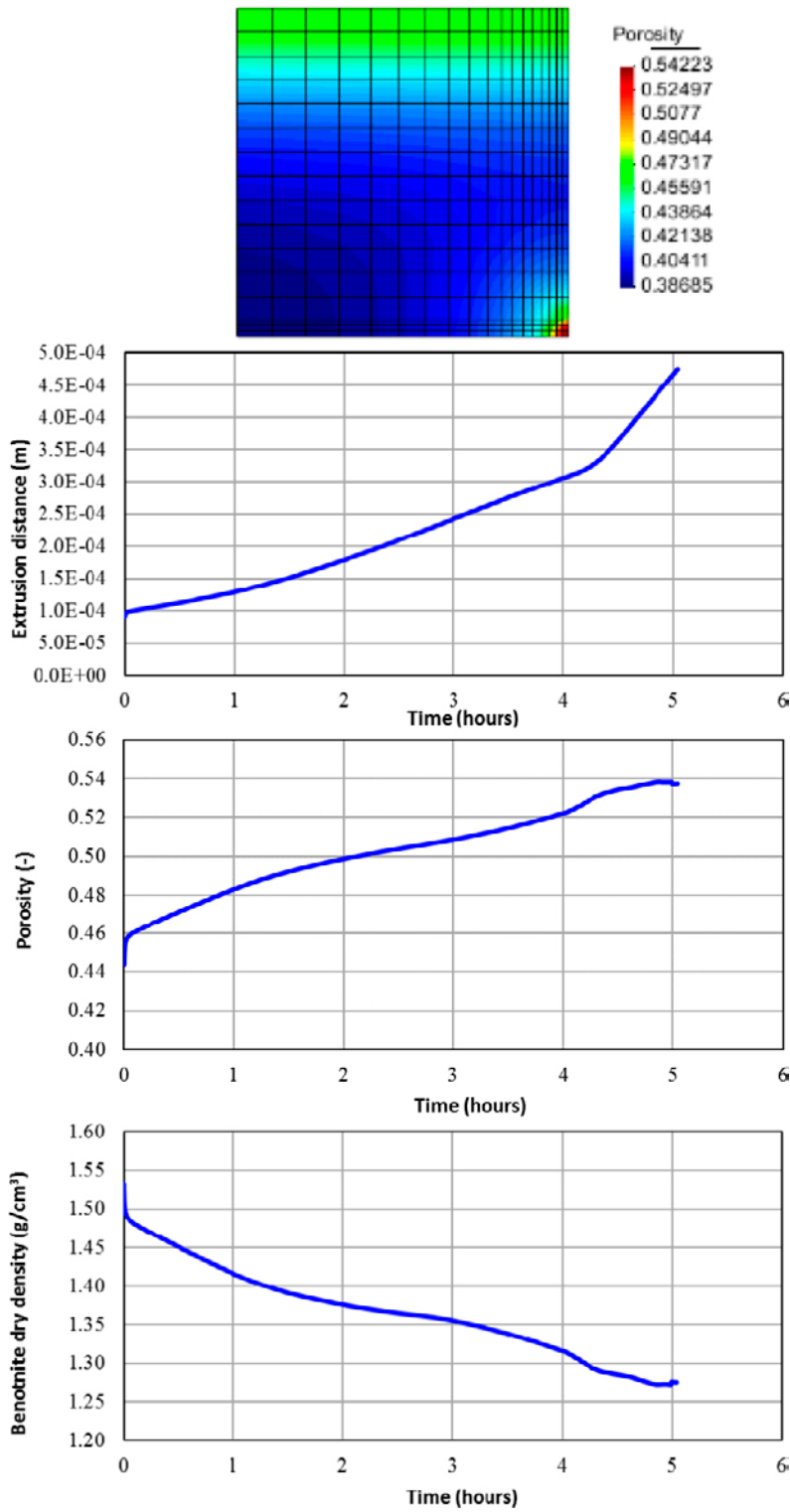


**Figure 4-13.** Porosity (-), horizontal displacement (m) and dry density (g/cm<sup>3</sup>) results for the clay block model after 5 h.

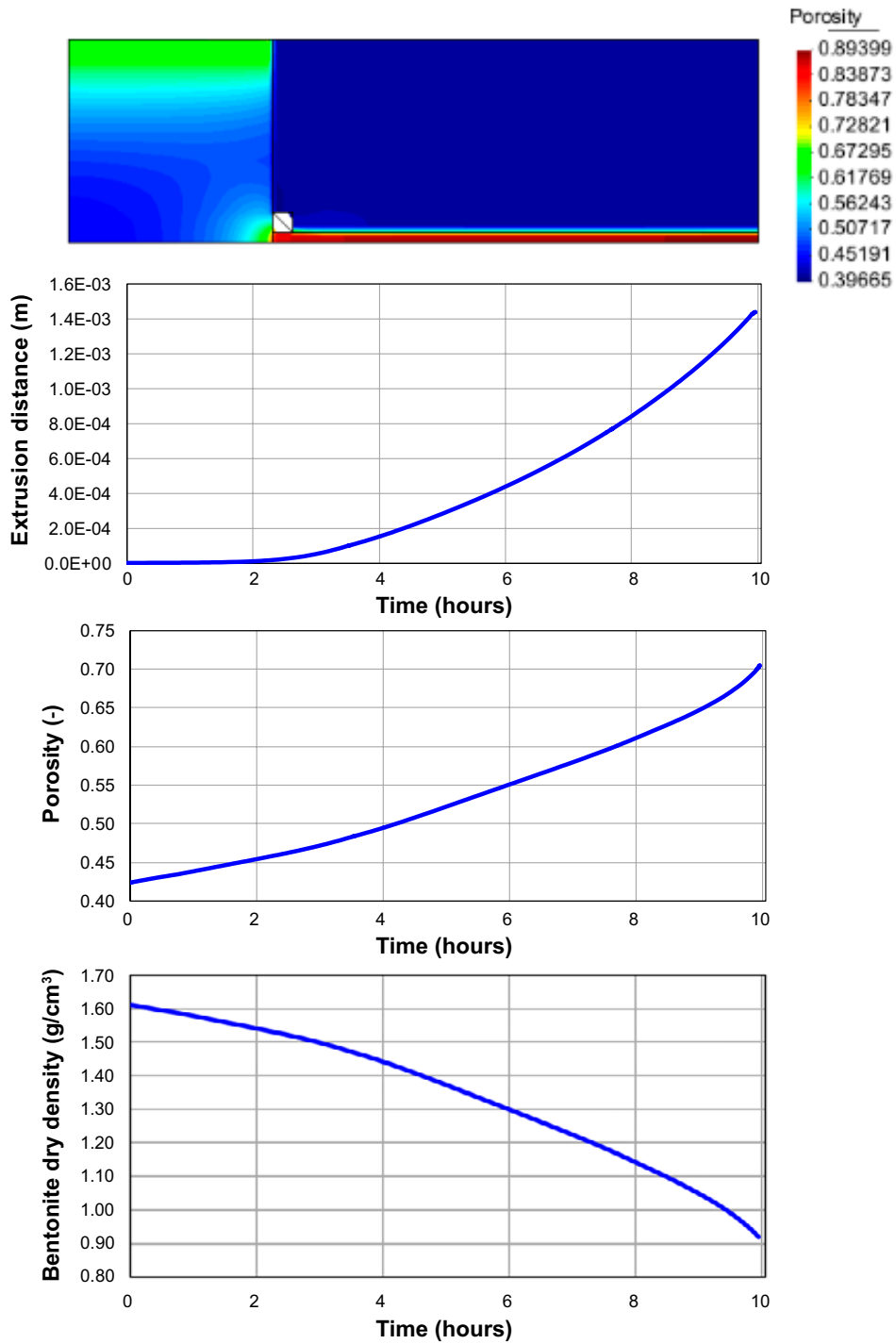


**Figure 4-14.** Porosity (-), horizontal displacement (m), and dry density (g/cm<sup>3</sup>) results for the complete cell model after 10 h.

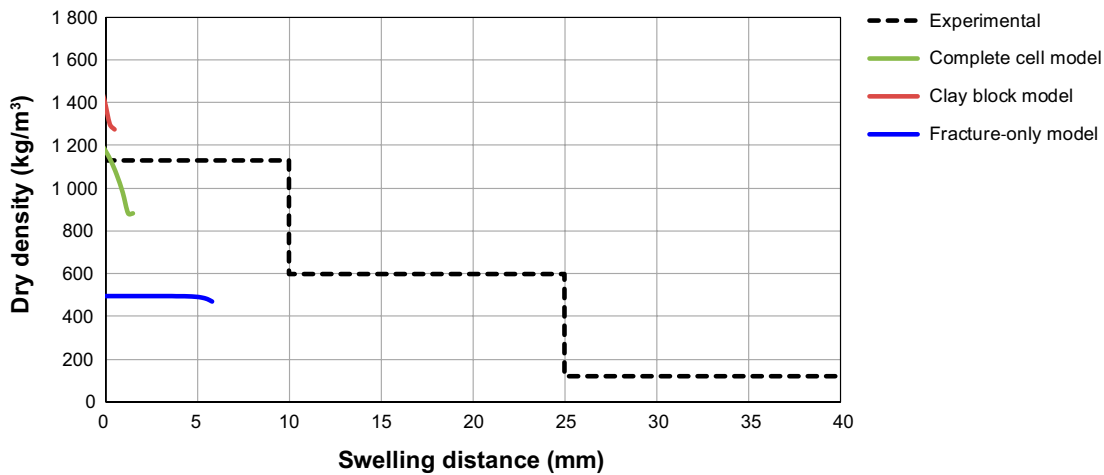


**Figure 4-15.** Comparison between the dry density ( $\text{kg/m}^3$ ) distribution as a function of swelling distance (mm) obtained at the end of the simulations with experimental observations from Schatz et al. (2013): experimental observations after 720 hours, fracture model after 10 h, clay block model after 5 h, and complete cell model after 10 h.

The results of the fracture model show a displacement of the bentonite-fracture interface of 5.77 mm after ~10 hours (Figure 4-12), much larger than the first trial model. The results show a nearly linear increase in porosity and extruding distance with time, with the corresponding dry density decrease. As it expands, porosity at the outermost bentonite point increases from the initial 0.42 to 0.83, equivalent to a void ratio of 5.25. The increase in porosity is translated into a decrease in dry density from the initial 1.59 to 0.46  $\text{g/cm}^3$ . The simulation stopped after almost 10 hours due to convergence issues in the constitutive model when reaching large deformations.

Results of the clay block model, presented in Figure 4-13, were only obtained for 5 hours of experiments due to similar numerical convergence issues. After this time, the extrusion distance is 0.475 mm, much lower than the displacement of the fracture-only model after 5 hours (~2 mm). This is mainly due to geometrical and boundary condition reasons. The corresponding porosity and bentonite dry density are 0.54 and 1.276  $\text{g/cm}^3$ , respectively. The extrusion of the whole bentonite block is only allowed through the fracture section (see boundary conditions in Section 4.4.1) and perfect contact is assumed between bentonite and the stiff acrylic domain. In contrast with the fracture model, where the extrusion process resembles a free swelling experiment, geometrical limitations of the model are highlighted in this set of results.

Figure 4-14 presents the complete cell model results. The main differences with the clay block model results are due to the incorporation of a less stiff acrylic material in the fracture-clay block interface, added in an attempt to limit the effect of the perfect contact between bentonite and acrylic (see Section 4.4.1). With this modification of the geometry, a simulation time of 10 hours could be calculated, at which time similar numerical convergence issues prevent the simulation to continue. The swelling process is much more advanced than in the clay block model, but still less intrusion is predicted compared to the fracture-only model (Figure 4-12). Results after 10 hours of extrusion predict a total displacement of the bentonite-fracture interface of 1.44 mm, with a maximum porosity of 0.77 and a bentonite dry density decrease to 0.92  $\text{g/cm}^3$ . As with the previous models, it is thought that in this case geometric limitations are also clearly playing an important role in limiting the extrusion distance and preventing the simulation to advance further after 10 hours.

The model and experimental results are compared in Figure 4-15 in terms of the dry density of the clay that has extruded into the fracture after each final simulation time and its comparison with experimental data after 720 hours from Schatz et al. (2013). The model results in Figure 4-15 consider the mass of bentonite that falls at the right of the initial position of the bentonite-fracture interface. However, it should be noted that the experimental results correspond to the final state of the experiment after 720 hours, while model results were only obtained for 10 hours at the most due to numerical convergence issues. This figure allows a quick comparison between maximum swelling distances obtained in each model. A quantitative comparison between these results in terms of dry density distribution is not possible due to the great differences in extrusion distances between model (5 to 10 hours) and experimental results (after 720 hours).

## 5 Conclusions and discussion

### 5.1 Conclusions of particle-based models

In cooperation with CIMNE (International Centre for Numerical Methods in Engineering), the feasibility of using the Discrete Element Method (DEM) to simulate the erosion of bentonite was assessed. The details of this work can be found in Section 3. In particular, the DEM as a way to study the development and erosion of the clay sol that forms at the rim region has been explored. The characteristic scales of the problem to assess the feasibility of this kind of approach have been studied. Difficulties in applying the direct approach were found, meaning the direct use of particles to calculate the erosion rate of clay at the rim region, under the influence of an incoming flow. The main issue with this kind of approach is the extremely long times needed to reach a sufficiently developed solution, or to reach steady-state conditions. Nonetheless, a set of numerical tools to adapt an existing CFD-DEM application to the problem at hand has been developed, including:

1. A new particle object to deal with the particular potentials and specific fluid-coupling characteristic of the clay particles.
2. A new integration scheme based on the velocities, given that the relaxation time of the particles is extremely low due to their extremely small mass.
3. A periodic version of the search algorithm and force calculation to be able to run periodic domains filled with sol.
4. A new type of inlet, the force inlet, which imposes an injection force to simulate the gel-sol interphase with a fixed solid fraction boundary condition.
5. A tool to calculate fluxes through surfaces.
6. A new set of filtering tools.
7. A new type of imposed fluid velocity based on the local viscosity.

Furthermore, an intermediate approach has been proposed as an alternative, consisting in studying upscaled properties for the macroscopic description of the system. Specifically, it has been shown how the diffusivity may be recovered from the system. It is proposed here that this could be an appropriate way to approach the problems. The diffusivities are consistent with the model of Liu et al. (2009a), except for a region with some noise that is attributed here to the extremely low values of the solid fraction gradient. Nevertheless, it is acknowledged that the presented technology in its current state is not sufficient to answer the difficult questions posed by Neretnieks et al. (2009, 2010, 2017) and that more developments would be needed for that. The most important ones are:

1. Development of flat coin-like or polyhedral particles to better model the real shape of the clay ones.
2. Assessment of the relevance of hydrodynamic interactions, which are only treated in an upscaled way in the present model, which is based on a static porous medium conception of the medium that might not be adequate upon closer inspections.
3. Exploration of several techniques to narrow down the range of scales present in the problem, including the telescoping down of scales and the stiffness softening of the potentials.
4. The consideration of implicit strategies that might speed up the simulations, especially as the process slows down as the rim region relaxes towards steady-state.

### 5.2 Conclusions of experiments and soil mechanics models

In Section 4, three bentonite expansion experiments have been simulated using the finite element code Code\_Bright (Olivella et al. 2016). The elastoplastic non-linear constitutive model used is the Barcelona Expansive Model (BExM) described in Alonso et al. (1999).

Two free vertical swelling experiments (Sane et al. 2013) have been first simulated to calibrate the hydro-mechanical (HM) model prior to the simulation of an extrusion experiment into a narrow slot

(i.e. a fracture). A good match between experimental and modelled results in terms of free swelling evolution with time has been obtained.

With the calibrated model, an experiment of the expansion of a bentonite sample and its intrusion into an artificial fracture (Schatz et al. 2013) has been simulated. Due to difficulties in numerical convergence of the constitutive model when reaching large deformations, it was only possible to simulate a short time of the total duration of the test with all the models. Numerical problems arise when very high porosity values are reached, leading to a maximum swelling in the order of few millimetres. Under those conditions, plastic deformations become considerably large. In combination with the geometrical constraints exerted by the fracture and acrylic domains, the algorithm fails to converge. With these geometrical and numerical constraints, the clay penetration into the fracture reach a maximum of 1.44 mm in the models. Considering the model that restricts the analysis to a bentonite layer with the same thickness as that of the fracture, expansions reach a maximum value of 5.8 mm after 10 hours. However, that simpler model also fails to converge after reaching this extrusion distance. Convergence issues in this work are related with the fact that the constitutive model and Code\_Bright are not intended to be used for solving this type of problem, involving extremely large deformations (several hundreds percent). Still, one of the goals of this work was to actually determine the limits of applicability of such soil mechanics models to this type of problems.

### 5.3 Multi-phase bentonite modelling based on macroscopic models as a potential way forward

The results obtained in this work show that the Barcelona Expansive model BExM used to model the expansive behaviour of MX-80 bentonite is only able to capture the observed deformations in its very first stage of expansion when contacting with water. Large swelling strains can be modelled if the bentonite micro-structure is considered in the model. Its volumetric deformation, while saturation increases, contributes to the total deformation of the macro-structure, which then evidence irreversible strains during swelling response (far from preconsolidation stress history of the material).

The numerical model reproduces well the results of the free swelling tests (sections 4.2 and 4.3). On the other hand, it fails to simulate the erosion test 11 of Schatz et al. 2013), only giving reasonable estimates during the first hours. Numerical instabilities of the non-linear constitutive law when reaching high values of porosity in the non-linear range together with geometrical constraints characteristic of the test have hindered the possibility of modelling the entire duration of the erosion experiments.

The deformations obtained from the model of the erosion test, although they represent significant deformations of the material, are too small compared the deformations observed in laboratory tests. This is to a great extent related to the transition of bentonite from solid to gel (a soft viscous material) in the experiments. This gel behaves rather as a viscous liquid. The physical behaviour of that gel seems to govern the evolution of the extrusion distance and is out of the scope of the behaviour of expansive clays explained by traditional soil mechanics models such as the BExM.

It is speculated here that this transition could be modelled by considering an additional differential equation that quantifies the evolution in time of the value of a phase parameter “ $x$ ”. This phase parameter would represent how much bentonite there is in the solid phase and how much in the liquid phase. This weight parameter would then proportionally affect the governing equations of the problem, given by:

- (a)  $x$  · momentum balance in terms of stresses and
- (b)  $(1-x)$  · mass balance of water.

Addressing the problem of phase transition (erosion) in this way would enable to model both: (1) the expansion of compacted bentonite and (2) the bentonite gel behaviour, in a simultaneous fashion as erosion progresses. However, this work would require the derivation of the theoretical formulation and the enhancement of numerical tools for a sound and robust numerical evaluation of the problem.

## References

SKB's (Svensk Kärnbränslehantering AB) publications can be found at [www.skb.se/publications](http://www.skb.se/publications).

**Alonso E E, Gens A, Josa A, 1990.** A constitutive model for partially saturated soils. *Géotechnique* 40, 405–430.

**Alonso E E, Vaunat J, Gens A, 1999.** Modelling the mechanical behaviour of expansive clays. *Engineering Geology* 54, 173–183.

**Birgersson M, Börgesson L, Hedström M, Karnland O, Nilsson U, 2009.** Bentonite erosion. Final report. SKB TR-09-34, Svensk Kärnbränslehantering AB.

**Boisson J Y, 1989.** Study on the possibilities by flowing ground waters on bentonite plugs expanded from borehole into fractures. In *Sealing of radioactive waste repositories: Proceedings of NEA/CEC Workshop*. Paris: OECD/NEA, 229–244.

**Brooks R M, Corey A T, 1964.** Hydraulic properties of porous media. *Hydrology Paper 3*, Colorado State University, Fort Collins, Colorado.

**Burdine N T, 1953.** Relative permeability calculations from pore size distribution data. *Journal of Petroleum Technology* 5, 71–78.

**Dadvand P, Rossi R, Oñate E, 2010.** An object-oriented environment for developing finite element codes for multi-disciplinary applications. *Archives of Computational Methods in Engineering* 17, 253–297.

**Durlofsky L J, Brady J F, 1989.** Dynamic simulation of bounded suspensions of hydrodynamically interacting particles. *Journal of Fluid Mechanics* 200, 39–67.

**Dvinskikh S V, Szutkowski K, Furó I, 2009.** MRI profiles over very wide concentration ranges: application to swelling of a bentonite clay. *Journal of Magnetic Resonance* 198, 146–150.

**Grindrod P, Peletier M, Takase H, 1999.** Mechanical interaction between swelling compacted clay and fractured rock, and the leaching of clay colloids. *Engineering Geology* 54, 159–165.

**Guo Y, Curtis J S, 2015.** Discrete element method simulations for complex granular flows. *Annual Review of Fluid Mechanics* 47, 21–46.

**Harjupatana T, Alaraudanjoki J, Kataja M, 2015.** X-ray tomographic method for measuring three-dimensional deformation and water content distribution in swelling clays. *Applied Clay Science* 114, 386–394.

**Hedström M, Ekvy Hansen E, Nilsson U, 2016.** Montmorillonite phase behavior. Relevance for buffer erosion in diluted groundwater. SKB TR-15-07, Svensk Kärnbränslehantering AB.

**Karnland O, Muurinen A, Karlsson F, 2005.** Bentonite swelling pressure in NaCl solutions. Experimentally determined data and model calculations. In Alonso E E, Ledesma A (eds). *Advances in understanding engineered clay barriers: Proceedings of the International Symposium on Large Scale Field Tests in Granite, Sitges, Barcelona, 12–14 November 2003*. London: Taylor and Francis, 241–256.

**Krantz W B, 2007.** *Scaling analysis in modeling transport and reaction processes: a systematic approach to model building and the art of approximation*. New York: AIChE.

**Kurosawa S, Kato H, Ueta S, Yokoyama K, Fujihara H, 1999.** Erosion properties and dispersion flocculation behavior of bentonite particles. In Wronkiewicz D J, Lee J H (eds). *Scientific basis for nuclear waste management XXII: symposium held in Boston, Massachusetts, 30 November to 4 December 1998*. Warrendale, PA: Materials Research Society. (Materials Research Society Symposium Proceedings 556), 679–686.

**LeVeque R J, 2008.** *Finite difference methods for ordinary and partial differential equations: steady-state and time-dependent problems*. Society for Industrial and Applied Mathematics (SIAM).

**Liu L, 2011.** A model for the viscosity of dilute smectite gels. *Physics and Chemistry of the Earth, Parts A/B/C* 36, 1792–1798.

- Liu J, Neretnieks I, 2006.** Physical and chemical stability of the bentonite buffer. SKB R-06-103, Svensk Kärnbränslehantering AB.
- Liu L, Moreno L, Neretnieks I, 2009a.** A dynamic force balance model for colloidal expansion and its DLVO-based application. *Langmuir* 25, 679–687.
- Liu L, Moreno L, Neretnieks I, 2009b.** A novel approach to determine the critical coagulation concentration of a colloidal dispersion with plate-like particles. *Langmuir* 25, 688–697.
- Maxey M R, Riley J J, 1983.** Equation of motion for a small rigid sphere in a nonuniform flow. *Physics of Fluids* 26, 883–889.
- Moreno L, Neretnieks I, Liu L, 2010.** Modelling of erosion of bentonite gel by gel/sol flow. SKB TR-10-64, Svensk Kärnbränslehantering AB.
- Moreno L, Neretnieks I, Liu L, 2011.** Erosion of sodium bentonite by flow and colloid diffusion. *Physics and Chemistry of the Earth, Parts A/B/C* 36, 1600–1606.
- Navarro V, Asensio L, Yustres Á, Pintado X, Alonso J, 2014.** An elastoplastic model of bentonite free swelling. *Engineering Geology* 181, 190–201.
- Navarro V, Asensio L, Yustres Á, De la Morena G, Pintado X, 2016.** Swelling and mechanical erosion of MX-80 bentonite: pinhole test simulation. *Engineering Geology* 202, 99–113.
- Navarro V, Yustres A, Asensio L, De la Morena G, Laurila T, Pintado X, 2017.** Modelling of compacted bentonite swelling that accounts for salinity effects. *Engineering Geology* 223, 48–58.
- Neretnieks I, Liu L, Moreno L, 2009.** Mechanisms and models for bentonite erosion. SKB TR-09-35, Svensk Kärnbränslehantering AB.
- Neretnieks I, Liu L, Moreno L, 2010.** Mass transfer between waste canister and water seeping in rock fractures. Revisiting the Q-equivalent model. SKB TR-10-42, Svensk Kärnbränslehantering AB.
- Neretnieks I, Liu L, Moreno L, 2017.** Clay erosion – impact of flocculation and gravitation. SKB TR-16-11, Svensk Kärnbränslehantering AB.
- Olivella S, Gens A, Carrera J, Alonso E E, 1996.** Numerical formulation for a simulator (CODE\_BRIGHT) for the coupled analysis of saline media. *Engineering Computations* 13, 87–112.
- Padding J T, Louis A A, 2006.** Hydrodynamic interactions and Brownian forces in colloidal suspensions: coarse-graining over time and length scales. *Physical Review E – Statistical, Nonlinear, and Soft Matter Physics* 74, 031402. doi:10.1103/PhysRevE.74.031402
- Pintado X, Mamunul H Md, Martikainen J, 2013.** Thermo-hydro-mechanical tests of buffer material. Posiva 2012-49, Posiva Oy, Finland.
- Pinyol N, Vaunat J, Alonso E E, 2007.** A constitutive model for soft clayey rocks that includes weathering effects. *Géotechnique* 57, 137–151.
- Pusch R, 1983.** Stability of bentonite gels in crystalline rock – physical aspects. SKBF/KBS TR-83-04, Svensk Kärnbränslehantering AB.
- Pusch R, 1999.** Clay colloid formation and release from MX-80 buffer. SKB TR-99-31, Svensk Kärnbränslehantering AB.
- Pusch R, 2007.** Colloids formed from buffer clay – nature and physical stability. Report. Geodevelopment International AB, Sweden.
- Sagaut P, 2002.** Large Eddy simulation for incompressible flows: an introduction. 2nd ed. Berlin: Springer.
- Samiei K, Peters B, Bolten M, Frommer A, 2013.** Assessment of the potentials of implicit integration method in discrete element modelling of granular matter. *Computers & Chemical Engineering* 49, 183–193.
- Sane P (ed), Laurila T, Olin M, Koskinen K, 2013.** Current status of mechanical erosion studies of bentonite buffer. Posiva Report 2012-45, Posiva Oy, Finland.

- Schatz T, Kanerva N, Martikainen J, Sane P, Olin M, Seppälä A, Koskinen K, 2013.** Buffer erosion in dilute groundwater. Posiva Report 2012-44, Posiva Oy, Finland.
- Schofield A N, Wroth C P, 1968.** Critical state soil mechanics. New York: McGraw-Hill.
- Sjöblom R, Kalbantner P, Bjurström H, Pusch R, 1999.** Application of the general micro-structural model to erosion phenomena – Mechanisms for the chemical-hydrodynamic conversion of bentonite to a pumpable slurry in conjunction with retrieval. *Engineering Geology* 54, 109–116.
- Solowski W T, Gallipoli D, 2010.** Explicit stress integration with error control for the Barcelona Basic Model. Part 2: algorithms efficiency and accuracy. *Computers and Geotechnics* 37, 1667–1681.
- Spellings M, Marson R L, Anderson J A, Glotzer S C, 2017.** GPU accelerated Discrete Element Method (DEM) molecular dynamics for conservative, faceted particle simulations. *Journal of Computational Physics* 334, 460–467.
- Tanai K, Matsumoto K, 2007.** A study on extrusion behavior of buffer material into fractures using X-ray CT method. In *Proceedings of 3rd International Meeting on Clays in Natural & Engineered Barriers for Radioactive Waste Confinement*, Lille, France, 17–20 September 2007.
- van Genuchten M T, 1980.** A closed-form equation for predicting the hydraulic conductivity of unsaturated soils. *Soil Science Society of America Journal* 44, 892–898.
- Varga Z, Wang G, Swan J, 2015.** The hydrodynamics of colloidal gelation. *Soft Matter* 11, 9009–9019.
- Verbeke J, Ahn J, Chambré P L, 1997.** Long-term behaviour of buffer materials in geologic repositories for high-level wastes. Report UCB-NE-4220, University of California, Berkeley.
- Whitaker S, 1999.** The method of volume averaging. Dordrecht : Kluwer Academic. (Theory and Applications of Transport in Porous Media 13)
- Williams J R, O'Connor R, 1995.** A linear complexity intersection algorithm for discrete element simulations of arbitrary geometries. *Engineering Computations* 12, 185–201.
- Williams J R, Perkins E, Cook B, 2004.** A contact algorithm for partitioning  $N$  arbitrary sized objects. *Engineering Computations* 21, 235–248.
- Zhang H, Liu S-G, Han Z, Zheng L, Zhang Y-B, Wu Y-Q, Li Y-G, Wang W, 2016.** A new algorithm to identify contact types between arbitrarily shaped polyhedral blocks for three-dimensional discontinuous deformation analysis. *Computers and Geotechnics* 80, 1–15.



### Analysis of the formulation proposed by Neretnieks et al. (2017)

In this appendix some possible inconsistencies found in the formulation are studied and summarised. The second, 'alternative' Equation 3-7 for the derivative of  $r_R$  seems to be incorrect: it is just a version of Equation 3-6 where the derivative of  $\varphi$  is considered negligible. To see this, note that Equation 3-2 can be rewritten as:

$$M = \varnothing V \Rightarrow \dot{M} = \varnothing \dot{V} + V \dot{\varnothing} \quad (\text{A-1})$$

where the dot notation for the time derivatives is used, the volume is named as  $V$  and  $\varnothing := \rho_s \varnothing_{\text{mean}}$ . Which is simply expressing the mass balance as a change on the boundary (first term) plus a change in the interior (second term). Thus,

$$V = \delta_{fr} \pi (r_R^2 - r_i^2) \Rightarrow \dot{V} = 2 \delta_{fr} \pi r_R \dot{r}_R \quad (\text{A-2})$$

Introducing this expression into Equation 3-4 and using

$$\dot{M} = N - 2N_{rim} = : N \quad (\text{A-3})$$

yields to Equation 3-6. Note that, therefore, Equation 3-7 can be obtained by the above relations by neglecting the interior change (which is probably reasonable, especially when it is claimed that both expressions were found to give the same results). That is, taking

$$\dot{M} = \varnothing \dot{V} \quad (\text{A-4})$$

which corresponds to the reasoning given in Section 3.3. It is however strange that this simplification is not mentioned as just that.

Another simplification is performed implicitly in Equation 3-9. This equation is an expression of Reynolds Transport Theorem (RTT), i.e.

$$\frac{d}{dt} \int_{\Omega(t)} \mathbf{f} dV = \int_{\Omega(t)} \frac{\partial \mathbf{f}}{\partial t} dV + \int_{\partial\Omega(t)} (\mathbf{v}^b \cdot \mathbf{n}) \mathbf{f} dA \quad (\text{A-5})$$

where  $\mathbf{f}$  is any vector or scalar. In the current case  $\mathbf{f} = \varnothing$  and

$$\Omega = [0, 2\pi] \times [r, r + dr] \times [\delta_{fr}] \quad (\text{A-6})$$

The first left-hand side term in Equation 3-9 is obtained after neglecting higher-than-0-order terms, while the right-hand side is equal to the first term on the right-hand side of the RTT (fixing the volume in time and taking out the time derivative yields the variation of mass in the fixed control volume, which is equal to the balance of diffusion fluxes as given in Equation 3-9). However, the second term on the right-hand side of the RTT is neglected without comment. Again, this seems possible since the speed of diffusion is likely greater than the speed of expansion, but it is strangely overlooked, given the level of detail provided.

The next step in the derivation of the evolution equation of the system is not without similar simplifications, being difficult its understanding. The arguments are somewhat unorthodox, mixing discretisation concepts with continuum concepts. The equation is now derived with more standard calculus starting with Equation 3-10, which is obtained from formally applying the chain rule to its left-hand side as

$$\frac{\partial A dr \varnothing}{\partial t} = A dr \frac{\partial dr}{\partial t} + dr \varnothing \frac{\partial A}{\partial t} \quad (\text{A-7})$$

Now, unlike in the document, the following equation is used

$$dr = \frac{\partial r}{\partial t} dt \quad (\text{A-8})$$

The notation is simplified by writing Equation 3-14 as

$$A(r) = 2\pi \delta_{fr} r = Cr \quad (\text{A-9})$$

Using these relations, together with Equations 3-9 and 3-10, the following equation is obtained:

$$Cr \frac{\partial r}{\partial t} dt \frac{\partial \phi}{\partial t} + Cr \phi \frac{\partial}{\partial t} \left( \frac{\partial r}{\partial t} dt \right) + \frac{\partial r}{\partial t} dt \phi Cr \frac{\partial r}{\partial t} = C \frac{\partial}{\partial r} \left( Dr \frac{\partial \phi}{\partial r} \right) \frac{\partial r}{\partial t} dt \quad (\text{A-10})$$

From which the  $C$ s and the  $dt$ s (note that the one in the second term can be moved outside the time derivative) can be crossed out. Doing so and employing the dot notation for the time derivatives yields:

$$r \dot{r} \phi + r \ddot{r} \phi + \dot{r}^2 \phi = \frac{\partial}{\partial r} \left( Dr \frac{\partial \phi}{\partial r} \right) \dot{r} \quad (\text{A-11})$$

Since, it is clear that under uniform scaling

$$\frac{\partial r}{\partial r_R} = \frac{r - r_i}{r_R - r_i} \quad (\text{A-12})$$

which yields Equation 3-11, that is

$$\ddot{r} = \frac{r - r_i}{r_R - r_i} \ddot{r}_R \quad (\text{A-13})$$

and

$$\dot{r} = \frac{r - r_i}{r_R - r_i} \dot{r}_R + \left( \frac{\dot{r}(r_R - r_i) - (r - r_i)\dot{r}_R}{(r_R - r_i)^2} \right) \dot{r}_R = \frac{r - r_i}{r_R - r_i} \dot{r}_R \quad (\text{A-14})$$

where the last equality follows because the second term on the right-hand side is null, as it is seen when substituting Equation 3-11. Substituting these relations in the equation above yields

$$r \left( \frac{r - r_i}{r_R - r_i} \dot{r}_R \right) \dot{\phi} + \left( r \frac{r - r_i}{r_R - r_i} \ddot{r}_R \right) \phi + \left( \frac{r - r_i}{r_R - r_i} \dot{r}_R \right)^2 \phi = \frac{\partial}{\partial r} \left( Dr \frac{\partial \phi}{\partial r} \right) \left( \frac{r - r_i}{r_R - r_i} \dot{r}_R \right) \quad (\text{A-15})$$

Dividing by the coefficient of the first term on both sides (note that this is also done in the document; it should be checked whether the obtained version is valid for null time derivative of the outer radius)

$$\dot{\phi} = \frac{1}{r} \frac{\partial}{\partial r} \left( Dr \frac{\partial \phi}{\partial r} \right) - \phi \frac{\dot{r}_R}{r_R - r_i} \left( \frac{\dot{r}_R}{\dot{r}_R^2} (r_R - r_i) - \frac{r - r_i}{r} \right) \quad (\text{A-16})$$

Note that in the document the first term in the parenthesis is 1. Therefore, it is still left to reconcile both analyses (the one here and the one in Neretnieks et al. 2017), since one of them must be wrong.



SKB is responsible for managing spent nuclear fuel and radioactive waste produced by the Swedish nuclear power plants such that man and the environment are protected in the near and distant future.

**skb.se**